Final Report

Diode laser sensor for scramjet inlets: final year report

S. O'Byrne, S. Wittig, J. Kurtz, Y. Krishna, C. Rodriguez, M. Aizengendler and J. Davies

University of New South Wales, Australian Defence Force Academy

AFOSR/AOARD Reference Number: AOARD-10-4075

AFOSR/AOARD Program Manager: Dr Rengasamy Ponnappan

Period of Performance: 03/2010 – 03/2011

Submission Date: 03/06/2011

Principal Investigator:
Dr Sean O'Byrne, University of New South Wales, Australian Defence Force Academy

Report Documentation Page

Form Approved
OMB No. 0704-0188

Public reporting burden for the collection of information is estimated to average 1 hour per response, including the time for reviewing instructions, searching existing data sources, gathering and maintaining the data needed, and completing and reviewing the collection of information. Send comments regarding this burden estimate or any other aspect of this collection of information, including suggestions for reducing this burden, to Washington Headquarters Services, Directorate for Information Operations and Reports, 1215 Jefferson Davis Highway, Suite 1204, Arlington VA 22202-4302. Respondents should be aware that notwithstanding any other provision of law, no person shall be subject to a penalty for failing to comply with a collection of information if it does not display a currently valid OMB control number.

1. REPORT DATE	2. REPORT TYPE	3. DATES COVERED
07 JUN 2011	**Final**	**13-04-2010 to 12-04-2011**

4. TITLE AND SUBTITLE	5a. CONTRACT NUMBER
Diode Laser Scramjet Inlet Sensor	**FA23861014075**
	5b. GRANT NUMBER
	5c. PROGRAM ELEMENT NUMBER
6. AUTHOR(S)	5d. PROJECT NUMBER
Sean O'Byrne	5e. TASK NUMBER
	5f. WORK UNIT NUMBER
7. PERFORMING ORGANIZATION NAME(S) AND ADDRESS(ES)	8. PERFORMING ORGANIZATION REPORT NUMBER
University of New South Wales,ADFA,Northcott Drive, Campbell, ACT,2600, Australia,NA,NA	**N/A**
9. SPONSORING/MONITORING AGENCY NAME(S) AND ADDRESS(ES)	10. SPONSOR/MONITOR'S ACRONYM(S)
AOARD, UNIT 45002, APO, AP, 96338-5002	**AOARD**
	11. SPONSOR/MONITOR'S REPORT NUMBER(S)
	AOARD-104075

12. DISTRIBUTION/AVAILABILITY STATEMENT

Approved for public release; distribution unlimited

13. SUPPLEMENTARY NOTES

14. ABSTRACT

This work presents test results of a diode-laser sensor for an axially symmetric inlet in a Mach 6 hypersonic flow facility. The conical inlet design presented here is more realistic than the flat plate design presented in the previous report, and is similar to the design that will be chosen as part of the Australian Space Research Program SCRAMSPACE flight test scheduled for 2012. The optical system was changed for this study to make the pitch and catch optics less sensitive to vibration, and to fit into a smaller volume than for the previous test. In addition, wavelength modulation detection was attempted with the system. Initial tests of the conical inlet design showed that it was not starting, as indicated using flow visualization images. The second version of the sensor has similar velocity sensitivity to the system used for the flat plate inlet test. The conical system was, however, still too susceptible to amplitude noise, which hinders the ability of the system to measure the free stream temperature or the angle of attack. Electrical problems with the log-ratio amplifier prevented temperature measurements for the vehicle. Preliminary vibration tests have shown that the problem is caused by independent motion between the laser and collimator when the tunnel fires. A preliminary design of a low-power lock-in amplifier for use in field experiments was completed, and tests with current inputs in place of photodiodes proved successful.

15. SUBJECT TERMS

Aerospace, Hypersonic Flowfield Measurements

16. SECURITY CLASSIFICATION OF:			17. LIMITATION OF ABSTRACT	18. NUMBER OF PAGES	19a. NAME OF RESPONSIBLE PERSON
a. REPORT **unclassified**	b. ABSTRACT **unclassified**	c. THIS PAGE **unclassified**	**Same as Report (SAR)**	**54**	

Standard Form 298 (Rev. 8-98)
Prescribed by ANSI Std Z39-18

Contents

Abstract

This work is the final report for the project begun with AOARD-08-4019, and completes the work presented in that 2010 report entitled 'Diode Laser Sensor for Scramjet Inlets'. This report, AOARD-10-4075, presents tests of a diode-laser sensor for an axially symmetric inlet in a Mach 6 hypersonic flow facility. The conical inlet design presented here is more realistic than the flat plate design presented in the previous report, and is similar to the design that will be chosen as part of the Australian Space Research Program SCRAMSPACE flight test scheduled for 2012. The optical system was changed for this study to make the pitch and catch optics less sensitive to vibration, and to fit into a smaller volume than for the previous test. In addition, wavelength modulation detection was attempted with the system.

Initial tests of the conical inlet design showed that it was not starting, as indicated using flow visualization images. The sensor was able to clearly differentiate between the unstarted and the started hypersonic flow. In addition, this report presents some comparisons of velocity and temperature data presented in AOARD-08-4019 with more recent total temperature and pitot pressure data obtained in the TUSQ facility, which shows that the diode-laser temperature and velocity measurements in AOARD-08-4019 are consistent with these measurements.

The second version of the sensor has a similar velocity sensitivity to the system used for the flat plate inlet test. The conical system was, however, still too susceptible to amplitude noise, which hinders the ability of the system to measure the freestream temperature or the angle of attack. Electrical problems with the log-ratio amplifier prevented temperature measurements for the vehicle. Preliminary vibration tests have shown that the problem is caused by independent motion between the laser and collimator when the tunnel fires.

A preliminary design of a low-power lock-in amplifier for use in field experiments was completed, and tests with current inputs in place of photodiodes proved successful.

1 Introduction and Motivation

This is the final report for a 3-year investigation into the development of a diode-laser-based sensor for the inlet of a supersonic combustion ramjet engine, designed to measure the speed and temperature of the inlet flow, as well as the angle of attack of the inlet. This report presents the work on this project performed in 2010 and published in the report AOARD-08-4019, 'Diode Laser Sensor for Scramjet Inlets' (O'Byrne 2010).

This investigation was motivated by a desire to know the inlet conditions during the flight test of a supersonic combustion ramjet engine. There are two reasons why such a measurement is desirable. First, accurate knowledge of the freestream conditions is an essential prerequisite for comparing against computational models the behavior of a supersonic combustion ramjet (scramjet) vehicle in flight. The combustion behavior of a scramjet is a strong function of the thermodynamic conditions of the flow entering the inlet (Curran et al. 1996), and even a small systematic error in the freestream conditions can significantly alter the combustion behavior in the engine. The second motivation for having an inlet sensor of this type is that it can form the basis of a control system for a scramjet engine (Furlong et al. 1998). Because the combustion behavior is so sensitive to the inlet conditions,

it becomes important to have a method of rapidly measuring both the inlet and exhaust conditions of the engine so that the engine management system can change operational parameters such as fuel injection flow rates and locations to maintain the most efficient combustion possible at all times.

Although the concept of the supersonic combustion ramjet has been known since 1958 (Weber and MacKay 1958, Ferri 1964), and this engine design is generally agreed to be the most promising air-breathing propulsion method available at present, the practical difficulties of initiating and maintaining supersonic combustion have been so great that there is still currently no aircraft that routinely flies using scramjet propulsion. Recently there have been a number of successful flight tests involving supersonic combustors, including the HyShot tests in 2002 (Boyce et al. 2003) and the NASA X43 tests in 2004(McClinton 2006). While these tests have shown that supersonic combustion can be achieved outside the controlled environment of the laboratory, they are very difficult experiments from an instrumentation point of view. Instruments designed to make measurements at these conditions must be small to fit into the test engine, and must be able to survive the high dynamic pressures and heat fluxes produced in hypersonic flight.

The expense and difficulty of arranging flight experiments indicates the importance of measuring the thermodynamic and fluid-mechanical state of the inlet flow, both in order to make accurate simulations of the flowfield within the combustor and, in the longer term, to form the basis of an inlet sensor for engine control. This is the motivation for the experiments described in this report.

Although laser-based techniques like coherent anti-Stokes Raman scattering (CARS) (Eckbreth et al. 1988, Vereschagin et al. 2001, Cutler et al. 2003, O'Byrne et al. 2007) and planar laser-induced fluorescence (PLIF) (Allen et al. 1993, McMillin 1993, McIntyre et al. 1997, Gruber et al. 2004, O'Byrne et al. 2005) have proved to be very useful in laboratory scramjet tests because of their nonintrusive, species-specific measurement capabilities, these techniques require large, expensive pulsed laser systems that cannot realistically be put onto a flight experiment.

The technique we have chosen for this sensor is tunable diode laser absorption spectroscopy. This laser-based method was chosen because it has a number of desirable properties.

- The technique is nonintrusive. Laser-based techniques like diode laser absorption spectroscopy do not require physical probes to be placed in a flow. This is a distinct advantage for measuring supersonic and hypersonic velocities over traditional sensors used for subsonic flow, such as pitot probes.

- The technique is species-specific. Much of the important information about a flow operating at high speed in a combustor relates to concentrations of individual species.

- The system presented in this report is small and inexpensive. Any measurement system in a scramjet flight test must overcome very stringent time and space limitations. Also, the flight experiment vehicles tend to not be reusable, so any measurement system has to be considered disposable. For both these reasons, a diode laser system is a much more realistic sensing option than some of the techniques that are routinely applied in ground-test facilities.

Table 1: Absorbance of water vapor and oxygen at different altitudes using the US standard atmosphere

	0 km Altitude		25 km Altitude	
Species	VMR [ppmv]	Absorbance [m^{-1}]	VMR [ppmv]	Absorbance [m^{-1}]
H_2O	8138	0.79	32.2	$4.1x10^{-5}$
O_2	$2.09x10^5$	0.025	$2.09x10^5$	0.006

- The apparatus has no moving parts. Given the potential for very high vibration and thermal loads, the measurement system must be physically and thermally robust. Diode laser spectrometers use lasers adapted from telecommunications applications, where similar characteristics are require for adequate performance in the field.

Section 1.1 will present a brief summary of the most important results in previous work that are directly relevant to the project, to put the work presented in this report into context.

1.1 Summary of Previous Research

Allen (1998) presents a summary of diode-laser-based absorption studies for several applications, including aeroengine sensing applications. Most of the applications of diode laser absorption spectroscopy in engines, as opposed to wind-tunnel models, have used water vapor as the absorbing species and distributed feedback diode lasers as the light source (Griffiths and Houwing 2005, Upschulte et al. 2000, Zhao et al. 2003, Chang et al. 2010). However, these tests tended to concentrate on the combustor behavior of the engine, where water vapor is produced in large quantities by the combustion processes. In the inlet of a supersonic combustion ramjet, the water vapor concentration is very low because of the low concentrations of water vapor at the flight altitude of a scramjet engine. According to Zander (1973), the volume mixing ratio (VMR) of water vapor in the atmosphere reduces from 8138 ppmv at ground level down to 32.2 ppmv at altitudes above 25 km, as shown in Table 1.

There have been other research projects that have used oxygen to make inlet measurements. Most of these have been used to make measurements in subsonic or transonic flows (Miller et al. 1996, Lyle et al. 2007). Miller et al. (1996) used a Fabry-Perot diode laser, while Lyle et al. (2007) used both distributed feedback (DFB) and vertical-cavity surface-emitting lasers (VCSELs) for their measurements, finding that the VCSELs gave better results for the controlled wind-tunnel tests, while the higher power of the DFB laser was necessary for the engine tests. Both studies used fiber-coupled lasers with paths crossing the inlets in an 'X'-shaped configuration,and both studies cite uncertainties in measured velocity within 1–2 %.

This report differs from these studies in that the sensor is specifically designed to be used in the inlet of a supersonic combustion ramjet vehicle, flying at very high speeds. The system uses a single VCSEL with a retroreflected multi-pass arrangement, which is necessary given the low density conditions. The low power of the VCSEL is compensated for by using free-space propagation for the beam,

rather than an optical fiber-coupled system. The ability to scan the laser over several transitions leads to the system being able to measure both temperature through the ratio of the signal strengths and velocity through the Doppler shift.

Previously, experiments were performed on the inlet of a two-dimensional inlet with a single wedge of 10° (O'Byrne 2010). These tests showed the feasibility of the sensor as a velocity sensor and explained the obstacles that needed to be overcome in order to be able to directly measure the angle of attack on the inlet as well as the speed and freestream temperature.

The method used in O'Byrne (2010) and explained in detail in O'Byrne and Wittig (2008) is based upon the fact that the effect of temperature variations along the absorbing laser's path on absorption for a number of oxygen absorption lines with different ground-state energies will be slightly different for each of the transitions. If the concentration of oxygen is constant, and the temperature variation with path length can be described simply using only a few parameters, the parameters can be fitted by measuring the absorption from several transitions. The technique was first developed by Sanders et al. (2001) for simple spatial temperature distributions in a three-zone air furnace. In this study the path lengths of the three regions were considered to be known and the oxygen concentration was constant. The temperatures in each of the three zones were treated as variables and used to achieve a best fit for the measured spectrum. This method was later extended by Webster et al. (2005) to a furnace with two unknown temperatures and an unknown hot path length, producing good fits to temperatures measured independently using a thermocouple. The scramjet flat-plate inlet can be considered as a system containing three regions, with three different temperatures, velocities and path lengths. These quantities, in turn, are known functions of two variables: Mach number and angle of attack, as described in O'Byrne and Wittig (2008).

This report extends on the development of the sensor described in O'Byrne (2010) for flight, including:

- Comparisons of the flat-plate inlet measurements presented in O'Byrne (2010) with more recent pitot pressure and total temperature measurements and computational simulations
- Testing a more realistic axially symmetric, conical converging inlet configuration
- Comparing wavelength modulation detection with the log-ratio detection used for the sensor
- Development of a prototype lock-in amplifier for the wavelength modulation detection
- Further examination of the effect of measurement noise on fitting for the angle of attack

More recently, successful flight tests of a different diode laser absorption sensor have been performed on a hypersonic flight test, as part of the HIFiRE scramjet flight test program, although these measurements were not performed on an engine inlet. The design of the sensor is outlined in Williams et al. (2006) and Barhorst et al. (2009), and the results of the flight test are presented in Brown and Barhorst (2011). On this flight, both direct absorption and wavelength modulation were used to scan along a single oxygen transition in the A-band at 760 nm using a DFB laser. This experiment is important in

p_0	T_0	p_∞	T_∞	u_∞	p_{pitot}
MPa	K	Pa	K	m/s	kPa
0.8 ± 0.08	550	600	68	900	30

Table 2: Freestream flow parameters for hypersonic tests.

that it successfully demonstrated the feasibility of using oxygen absorption in hypersonic flight experiments. Again, an 'X' configuration of beams was used for the measurement, which was performed in a channel on the outside of the HIFiRE 1 test vehicle. Although this configuration is ubiquitous, the retroreflecting arrangement used in the present study has the advantage of keeping the same line of sight for both beam orientations, particularly in cases where the angle of attack of the vehicle is non-zero, which is not the case for the 'X' arrangement. Because this system uses retroreflectors, the beams are also forced to be anti-parallel to each other.

2 Test Facility and Flow Conditions

The hypersonic inlet tests were performed in the University of Southern Queensland's free-piston-driven Ludwieg tube facility (Buttsworth and Smart 2010). This facility has a number of properties that make it well suited to the development of a diode-laser-based oxygen sensor. As it is a very new facility, the flow has not been adequately characterized, which means that this method can provide useful time-resolved data about the inlet freestream conditions. Also, because the facility operates at lower total enthalpy conditions than shock tunnels, the duration of the flow is considerably longer. In the TUSQ tunnel, the flow duration is 0.2 seconds, some 200 times longer than the test time of the T-ADFA facility. Because the laser scan rate is limited to 200 Hz or less by the 50 kHz bandwidth of the log102 log-ratio detector, the duration of flow in the Ludwieg tube allows some 15–20 scans to be obtained during a run, which provides valuable time history data for the flow. Finally, because the freestream temperature is approximately 60 K, the transition strengths are high, and the signal-to-noise ratio of the absorption signal is significantly higher than it would be in a higher-enthalpy facility.

The tunnel consists of a 16-m-long Ludwieg tube connected to a nominally Mach-6 hypersonic nozzle. A high-pressure air reservoir providing an initial pressure of 20 MPa drives the piston down the tube, compressing the air in front of the piston until the single diaphragm located at the nozzle entrance ruptures and allows the gas to flow through the nozzle into the test section. The flow conditions generated at the nozzle reservoir and nozzle exit are summarized in Table 2.

The uncertainty in the total pressure is due to the variability in the measured pressure i nthe nozzle reservoir. There are several high-frequency fluctuations in the nozzle reservoir pressure, which was measured using a piezoelectric pressure transducer. These fluctuations are due to the complex system of compression and expansion waves traveling along the Ludwieg tube and the nozzle. During the 0.2-second test time, the average nozzle reservoir pressure increased from 830 kPa to 890 kPa, as can be seen in Fig. 1.

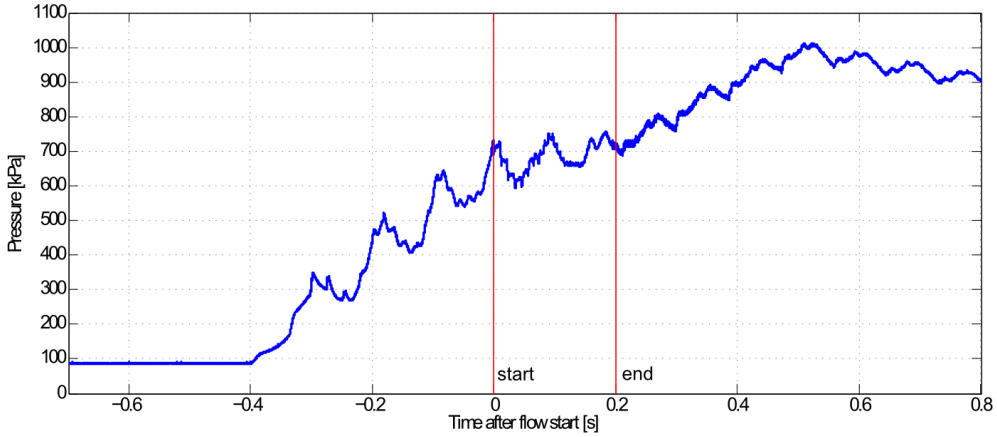

Figure 1: TUSQ nozzle reservoir pressure trace

Although the inviscid Mach number of the nozzle is 6.0, the displacement thickness of the boundary layer reduces the Mach number to approximately 5.8. Propagating the uncertainty in stagnation pressure, temperature and Mach number produces an uncertainty in the nozzle exit conditions in Table 2 of approximately 15 %.

In addition to the nozzle reservoir pressure, more recent results have been provided for the stagnation temperature in the TUSQ facility, which has been measured using thermocouple measurements (Buttsworth and Widodo 2010). The time-evolution of the total temperature is shown in Fig. 2. This plot shows that the total temperature is relatively constant over the first 0.14 s of the flow time, but that the temperature drops rapidly thereafter. The average stagnation temperature of approximately 490 K is significantly lower than the value of 571 K obtained by assuming isentropic flow behavior in the nozzle. This difference is attributed to conductive heat loss to the tube and nozzle walls during the compression process.

3 Optical System for Inlet Absorption Measurements

The optical system used for the measurements has been described previously in O'Byrne (2010), but is reproduced in Fig. 3. It consists of a VCSEL (Oclaro APC1101010809), whose supply current is adjusted using a Thorlabs LDC200 current controller and whose temperature is regulated using an on-chip Peltier cooler controlled using a Thorlabs TED200 PID-based temperature controller. The current for the diode is modulated using a voltage ramp generated using an Agilent 33220A arbitrary function generator. The frequency for the ramp determines the scan rate of the laser, and was set to 150 Hz for these measurements.

The light from the laser is collimated using an aspheric lens to a $1/e$-diameter of 2.5 mm. The beam is polarized by a prism to remove any polarization modulation due to changes in diode temperature or current, and passes to a second polarizing prism that splits the intensity of the laser light such that equal intensities reach the two 10 mm$\times$10 mm silicon PIN photodetectors. Adjusting the angle of the first prism allows fine control over the splitting ratio of the two beams. One of the beams

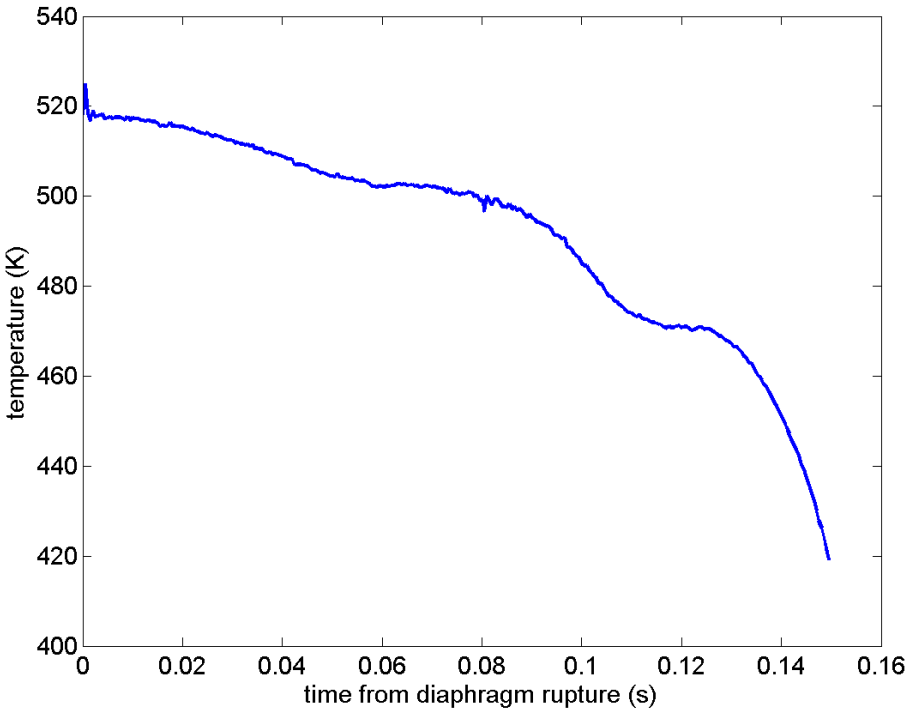

Figure 2: TUSQ total temperature measurement during the test time

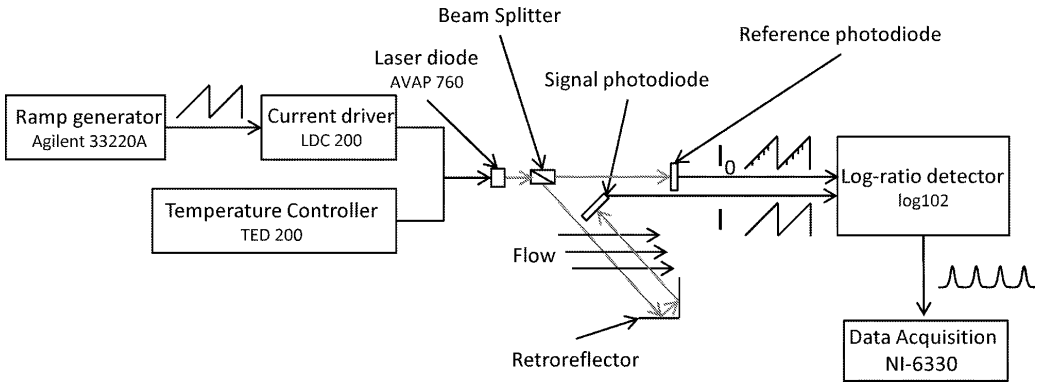

Figure 3: Schematic of TDLAS system

passes between two opposing retroreflectors. These retroreflectors have a lateral displacement between them that allows the beam to pass through the inlet multiple times, increasing the path length for the measurement. A maximum of 6 passes was possible using the flat-plate arrangement. The retroreflectors, called the dual-retroreflector apex-injected laser (DRAIL) system, ensures that the counter-propagating beams are always parallel to one another as they pass through the inlet. Because there will be equal numbers of beam passes with direction components towards and away from the freestream flow direction, the spectrum will contain two absorption peaks for each absorption line. The separation of these peaks is directly proportional to the velocity component in the direction of the laser beam, as described in O'Byrne (2010).

The photocurrent signals from the two photodiodes are inputs to a log-ratio amplifier circuit based around the Texas Instruments LOG102 amplifier. The output of the log-ratio detector is then further amplified, providing a voltage that is directly proportional to the absorbance. When the intensities of

the two laser beams are identical, the amplifier produces a null output. Once oxygen absorbs the light along the signal beam path, the output changes with the absorbance.

The output of the log-ratio amplifier is sampled by a National Instruments PCI6115E digitizer card. This card has a maximum sample rate of 10 MSPS and a 16-bit dynamic range. The data is acquired during the test for subsequent processing.

Measured spectra are fitted to computed spectra generated using the GENSPECT (Quine and Drummond 2002) line-by-line code and in-house nonlinear least-squares fitting routines. The spectral constants are obtained using the HITRAN2004 (Rothman et al. 2005) database. The in-house routines allow the data to be fitted for either velocity or temperature, or for both parameters.

This experimental arrangement and spectral fitting method were used for both the flat-plate inlet measurements and the conical inlet measurements. The two arrangements differed only in the inlet shape and in the method for mounting the optical components, and in a slightly more advanced log-ratio detector being used for the conical inlet measurements.

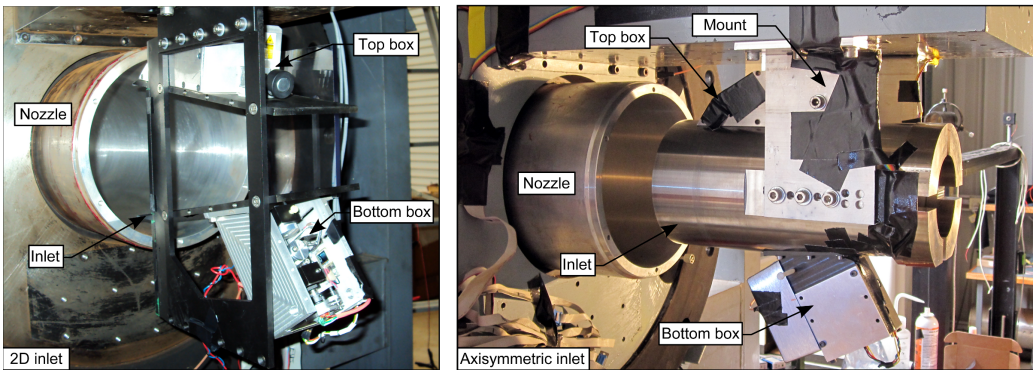

Figure 4: Flat-plate (left) and conical (right) experimental models

The structural differences between the flat-plate model used in O'Byrne (2010) and the conical model described in this report are apparent from Fig. 4. This figure shows both models as they were installed in the TUSQ facility. The image on the left shows the flat-plate model, while the image on the right shows the conical model. Sections 3.1 and 3.2 will discuss the designs of the two inlet models used for the experiment in detail.

3.1 Flat Plate Model

A cross-section of the model used for the flat-plate tests is shown in Fig. 5. The red lines in the figure indicate the path of the retroreflected laser beams. All of the optical components, with the exception of one of the retroreflectors, are placed in a box underneath the lower inlet plate, while that retroreflector is placed above the upper plate, on a platform containing a micrometer adjustment. The micrometer allows the spacing between the beam paths to be controlled. Smaller spacings allow more passes through the inlet.

The log-ratio amplifier board is located under the lower box, close to the box, to minimize the high-frequency noise that can be coupled into the photocurrents by using long cables connecting the pho-

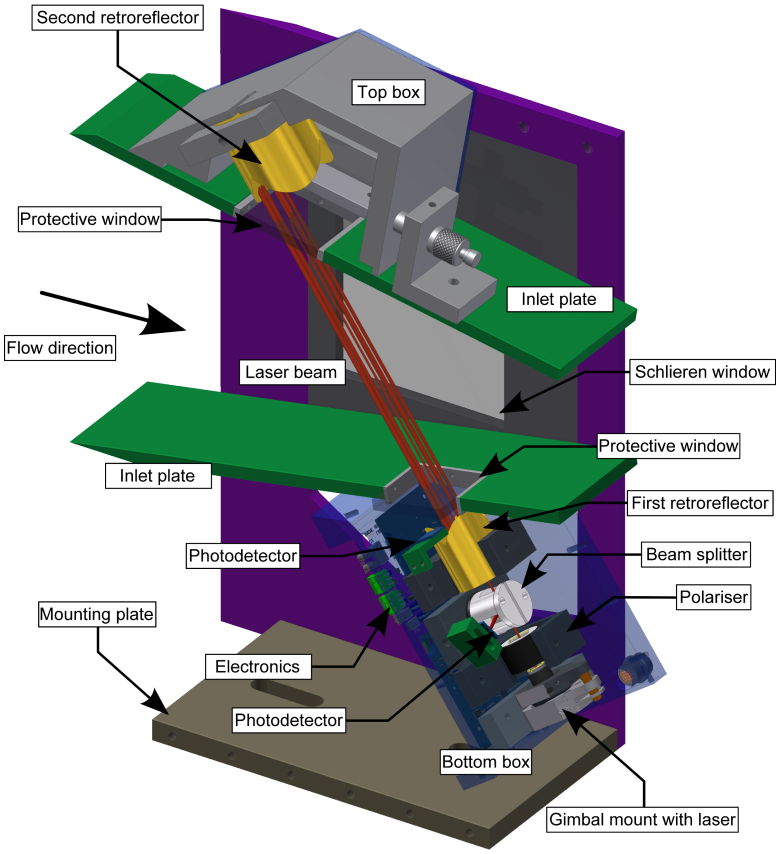

Figure 5: Flat-plate model cross-section

todiodes to the board.

The photodiode closest to the lower window is the signal detector, while the reference photodiode is nearest the cylindrical beamsplitter housing. The reference beam has a much shorter 2 cm path length than the signal beam. As the TUSQ facility is an impulse facility, with a total flow duration of only 0.2 s, and because the test section of the tunnel is evacuated to below 600 Pa before the test, the absorption due to this reference beam is considered negligible. The VCSEL is mounted on a Newport miniature gimbal mount, to allow for fine adjustment of the beam position.

The temperature controller, signal generator, current controller and data acquisition system were all located outside the test section of the facility. This was the case for both the flat-plate and conical inlet experiments.

3.2 Conical Inlet Model

A conical inlet has been designed for use as a more realistic flight test configuration than the original flat-plate inlet prototype. The lessons learned from the previous design were used to design a smaller, simpler and more robust sensor for flight. An axially symmetric geometry was chosen for the inlet because this geometry had previously been chosen for the inlet on the Australian Space Research Program's SCRAMSPACE flight test, upon which we intend to place a sensor of the type presented in

this study. Figure 6 shows the general structure of the conical inlet and the diode laser sensing system used to measure the flow conditions within the inlet.

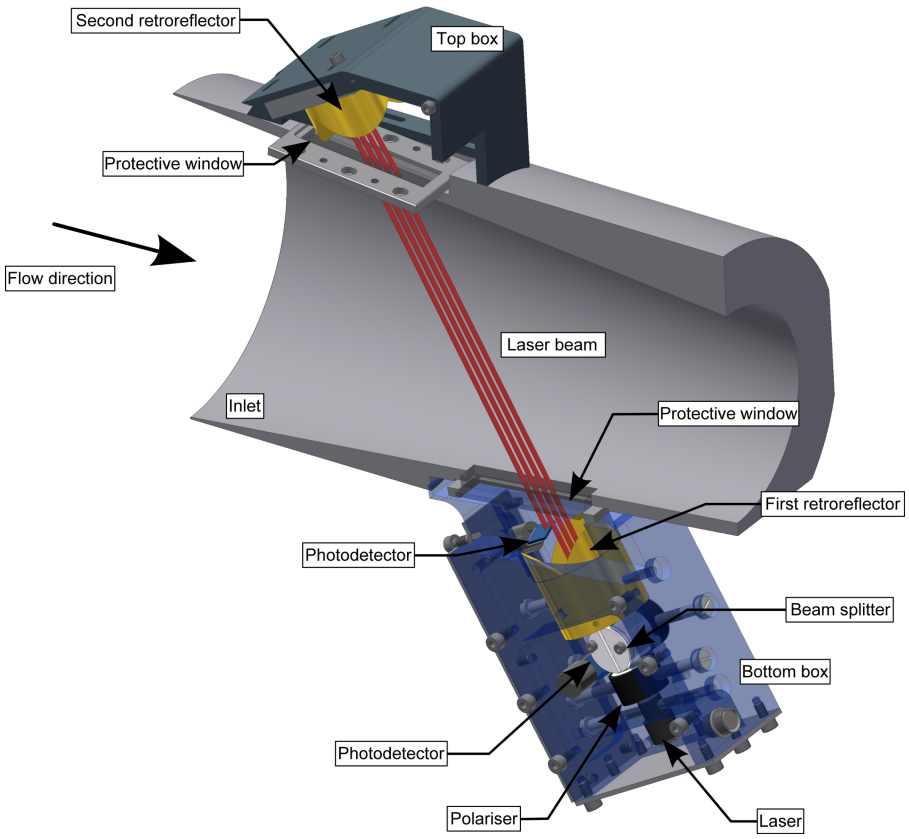

Figure 6: Conical model cross-section

The signal generation and detection methods for the conical inlet are the same as those used for the flat-plate inlet, described in Fig. 3. The retroreflector is still located in a separate box on the opposite side of the inlet, with the remaining components in the lower box. The Thorlabs current and temperature controllers used for the flat-plate tests were replaced with a Newport 501B current controller and Newport 350B temperature controller, which had superior current noise and temperature stability specifications, respectively.

The change from a 2D flat-plate inlet to a conical inlet made a redesign of the optical access to the inlet necessary. As the windows can no longer be flush with the inlet because of the circular inlet cross-section, steps inside the inlet are created where the inlet meets the window. These surface discontinuities could interfere with the flow and generate shock waves or trip the boundary layer. In order to reduce these possible flow interferences, the step height therefore must be kept to a minimum. Therefore the beam plane was rotated by 90 °. Figure 7(b) compares the beam orientations for the 2D inlet and the conical inlet arrangements. This complicates the analysis of the absorption signal, as the laser beam no longer passes through a field with homogeneous conditions and each beam now has a different path length, but reduces the step height to 1.2 mm. Using first-order compressible boundary layer theory and the computed flowfield, this step height should be well inside the boundary layer with an estimated thickness of 3.2 mm at the window located closest to the leading edge.

Figure 7(a) shows a comparison of the bottom box design for the or the 2D inlet and the conical

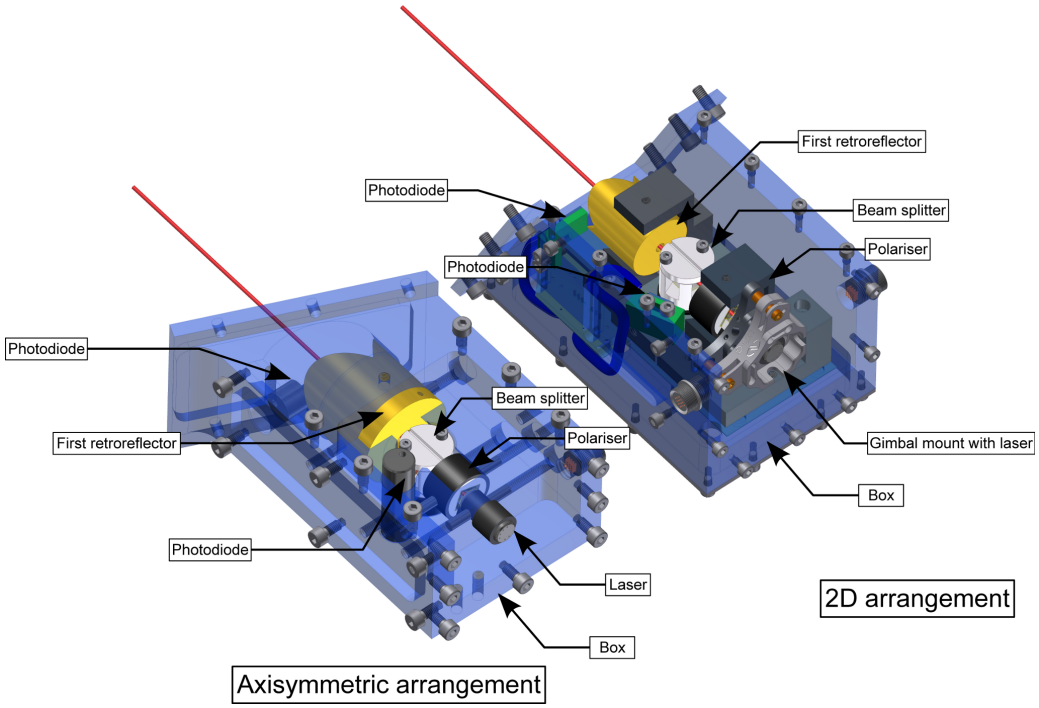

(a)

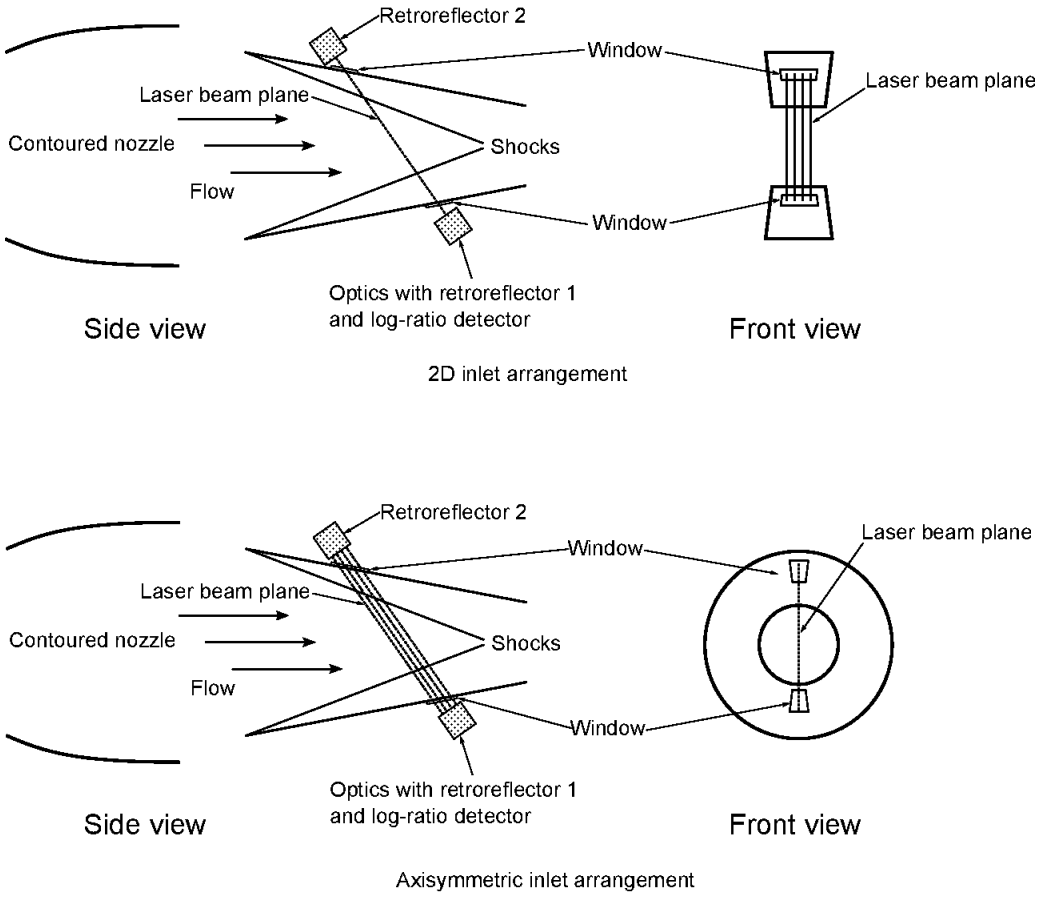

(b)

Figure 7: Comparison between (a) flat-plate and conical optical components and (b) beam orientations for the two configurations

inlet arrangement. The design of the bottom box which contains the laser, polarizer beam splitter, reference and signal photodetectors and the first retroreflector as part of the DRAIL system changed

from single components separately mounted in a hollow box to a solid aluminum block with spaces milled out for the optical components. This reduces the number of additional mechanical components such as screws and mounts which, in turn, reduces the number of degrees of freedom in the system and its components, and thus should reduce susceptibility to vibration and provide better and more stable alignment of the optical components. The reduction in the number of mechanical components also reduces potential points of failure. This is especially important for an in-flight test. Mounting of the two photo detectors was changed from being glued to a flat surface in the flat-plate configuration to a rotatable cylinder in a hole, again to provide for more precise and stable positioning of the photodiodes.

The mechanism for positioning and fixing the top box was changed from magnets and a micrometer adjustment to tie-down screws, providing more accurate and stable positioning of the second retroreflector. The size of the top box was reduced from 128×99×60 mm to 122×80×48 mm, which resulted in a weight reduction from 514 g to 379 g. The size of the bottom box was reduced from 135×100×62 mm down to 122×80×48 mm in preparation for the future flight-test, which would require further miniaturization. Despite the change to a single-block design and the use of a larger retroreflector, the weight of the bottom box only increased by 20 % from 768 to 923 g and the total volume including top and bottom box was reduced by 40 % from 1269 to 793 cm^{-3}.

The total weight including inlet, optical system, mounting brackets increased from 8 kg for the flat-plate inlet to 15 kg for the conical inlet. 94 % of this mass increase results from the conical inlet itself. A higher total mass together with the single-piece construction of the conical inlet should have a dampening effect on low-frequency mechanical vibrations.

The use of a larger first retroreflector (38.1 mm in diameter, compared with 25.4 mm for the flat-plate model) increased the maximum number of beam passes through the inlet from 6 for the flat-plate inlet to 12 for the conical inlet. This would allow a maximum path length of 1711 mm for the conical inlet compared to 742 mm for the 2D flat-plate inlet. For the present experiments the number of passes for both arrangements was limited to 4 as it was found that an increase in passes resulted in an increased susceptibility to mechanical vibrations. As the distance between the beams decreases with an increase in the number of passes, the beams are more susceptible to clipping occurring at the edges of the retroreflectors and/or the signal photodiode. The four passes resulted in a total path length of 494.8 mm for the flat-plate inlet and 563.5 mm for the conical inlet. The distance between beams was 6 mm for both configurations, and the $1/e$ diameter of the beam was 1.5 mm for the conical inlet tests.

Table 3: Comparison between 2D flat-plate inlet and conical inlet arrangement

Arrangement	ψ	n_{max}	d_{max}	θ	Volume	Mass
Unit	°		mm	°	cm^3	g
2D flat-plate	55.0	6	742	10	1269	1282
Conical	60.5	12	1711	7.2	793	1302

In Table 3, ψ is the angle between laser beam and freestream, θ is the angle to the center line, n_{max} is the maximum possible number of passes and d_{max} is the maximum path length. Volume and mass denote the totals for each optical system, including top and bottom boxes.

The detection electronics were also improved for these measurements. A new log-ratio amplifier board was constructed, with special attention paid to the use of low-noise components and better shielding using ground planes. The detector board was repositioned to reduce the cable length between the detector and the photodiodes from 12 cm to 5 cm, to help reduce RF noise pick-up from the photodetector cables between the PIN photodiodes and the amplifier board.

Figure 7(b) shows the most significant difference between the two sensing arrangements. The flat-plate model had the four laser beams separated in a direction perpendicular to the flow direction, because when the beams are oriented in this way they all pass through identical flow conditions, regardless of the angle of attack of the vehicle. This is impossible to achieve with the conical inlet geometry, for two reasons. First, if the beams are separated in a direction perpendicular to the flow axis, they would all experience significantly different flow conditions. At zero angle of attack, the flowfield that the beams pass through would look like an ellipse, with the outer portion of the ellipse containing the shock layer and the inner portion containing the freestream. Each of the beams would pass through a different chord of the ellipse. Also, a flat window that allowed the several beams to all pass through it would require a very deep cavity in the nozzle if it were oriented transverse to the flow axis, disturbing the inlet flow. For these reasons, the four beams in the conical inlet configuration were displaced in the axial direction. Although the beams will still experience slightly different flow conditions, the changes are much smaller in the axial direction than in the perpendicular direction. Also, by using a very narrow window, the size of the step generated by the window can be kept smaller than the boundary-layer thickness, as mentioned previously.

The choice of a conical nozzle for these tests therefore significantly complicates the analysis of the absorption signal. Rather than having only three flow regions with constant temperature and pressure in all three, the flow conditions will vary significantly through the two conical shock layers, and the path lengths occupied by those shock layers will be different for each of the beam passes, even for the simplest case of zero angle of attack. For any non-zero angle of attack or yaw, the flow becomes three-dimensional, and the conditions can only be determined by computationally intensive CFD calculations. In principle, the absorption profile will still be a function of Mach number and angle of attack, but if such fits are to be made, a large database of absorption spectra based on many three-dimensional computations would need to be generated. Conceptually, the approach is the same as for fitting the analytical results for the flat-plate inlet, but the flow conditions along each of the beam paths must be generated computationally rather than analytically, and the laser path must be divided into a large number of sections, in each of which the flow properties can reasonably be considered constant.

4 Computation of the Inlet Field

The temperature map for the flat plate inlet configuration is shown in Fig, 8. Computations for both the flat-plate and conical inlet configurations at zero angle of attack were performed using the computational fluid dynamics (CFD) code ANSYS FLUENT. These calculations were performed to determine how well the analytical solution for the flowfield outlined in O'Byrne and Wittig (2008) describes the

flowfield despite not modeling viscous effects in the flow, and to compare the contributions of the freestream and shock layers for the two inlet configurations, both for the cold TUSQ flow conditions and for possible flight testing.

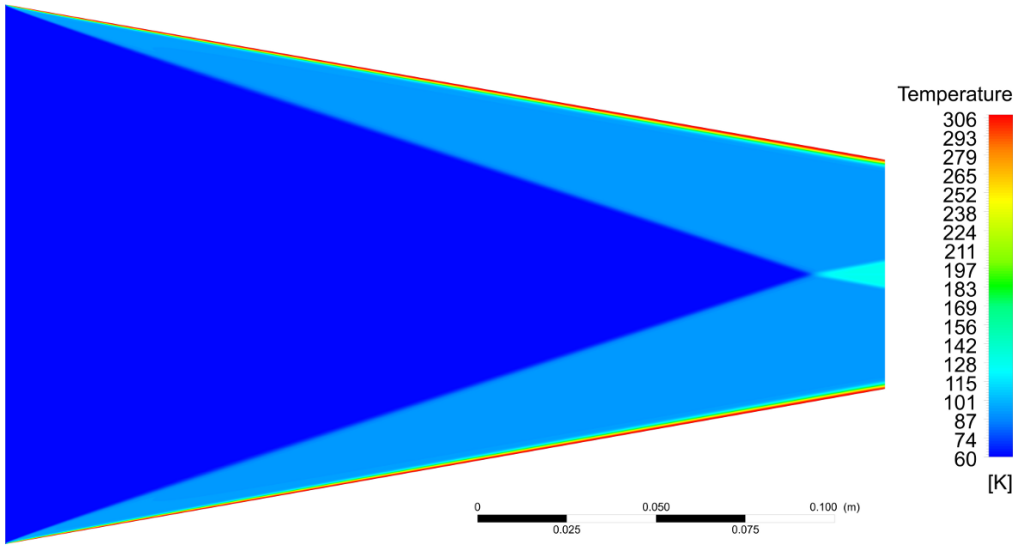

Figure 8: Temperature plot of the inlet flow for the flat-plate configuration

The FLUENT solver was set to implicitly solve the density-based form of the compressible Navier-Stokes equations, assuming perfect gas behavior. This is a reasonable assumption both for flight conditions and for the cold hypersonic conditions produced in the TUSQ Ludwieg tube. The boundary layers in the flow were also assumed to be laminar, which is a reasonable assumption at these flow conditions. The maximum Reynolds number at the exit of the flat plate inlet is approximately 500 000, around half the transition Reynolds number for a flat plate in hypersonic flow (He and Morgan 1994).

The solutions presented here used a rectangular grid for the interior of the computed flowfield. Grid convergence studies were performed for both inlet configurations, and showed insignificant variation in the solution parameters if more than 65 000 grid cells were used.

It is clear from Fig. 8 that the boundary layers are very thin relative to the shock layers and the freestream. At these high speeds and for the low TUSQ freestream temperature, temperatures within the boundary layer are elevated above the freestream temperature. The wall temperature, here assumed to be 300 K, is also higher than the freestream temperature. As the pressure within the boundary layer is, to a good approximation, constant, the density will decrease within the boundary layer. Thus, the boundary layers should contribute even less to the total absorption signal than their relatively small thickness would indicate. It is for this reason that the analysis of the effect on the spectrum of the angle of attack and Mach number can be considered accurate, despite not accounting for the boundary layer thickness.

The effect of the assumption of no boundary layer can be directly evaluated by calculating the absorption from the CFD-generated flowfield and comparing it to the absorption spectrum generated using the analytical model in (O'Byrne and Wittig 2008).

Figure 9 shows plots of absorbance along a single pass through the inlet, using the CFD results and the

analysis of O'Byrne and Wittig (2008) for the TUSQ freestream conditions. The inviscid calculation overpredicts the absorbance by only 3 % at the peak. Given the much faster calculation of flow conditions with varying angle of attack, and the low signal-to-noise ratios of the experiments, this is a very acceptable systematic error.

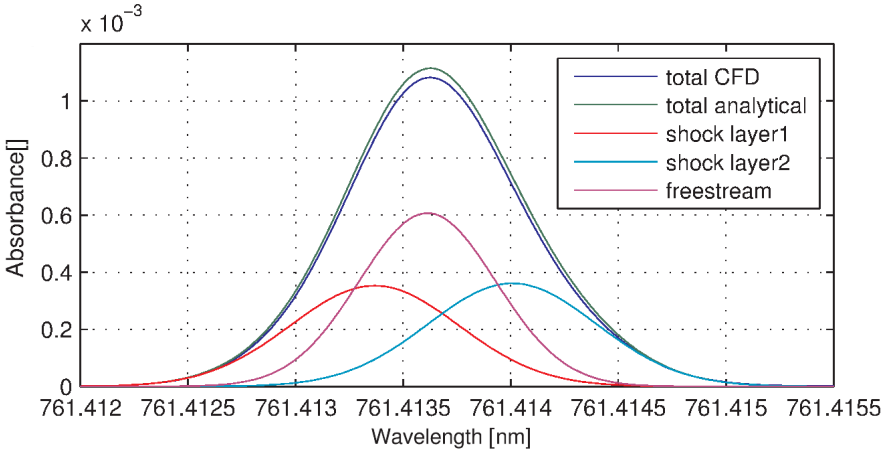

Figure 9: Absorbance for flat plate configuration comparing analytical with computed absorbance at the TUSQ freestream conditions

Comparing the relative contributions from the shock layers and the freestream in Fig. 9 to those at Mach 8 flight conditions presented in O'Byrne and Wittig (2008) shows that the TUSQ flow conditions have much more equal contributions from the freestream and the two shock layers than occurs in the upper atmosphere. This is because of the lower temperatures in the TUSQ freestream. The post-shock temperatures will increase as the freestream temperature increases, and because the absorption coefficient for the oxygen A band decays exponentially with temperature, the relative size of the contribution from the shock layers to the freestream tends to decrease as the freestream temperature increases. This indicates that the sensitivity to angle of attack will be lower in flight than at the facility conditions, and that the absorption spectrum from the flight test will be mostly due to the absorption contribution of the freestream.

4.1 Computation of the Conical Inlet Conditions

The conical inlet conditions have also been calculated for zero angle of attack, using ANSYS FLUENT, making the same assumptions of perfect gas, laminar flow used for the flat-plate inlet computations. As calculations were performed at zero angle of attack, the solver was able to be set to 2D axially symmetric, which significantly reduces the computational time compared to a fully three-dimensional flowfield calculation. Unlike the flat-plate inlet, however, any angle of attack on the conical inlet will generate three-dimensional flow, which, as stated previously, is a much more challenging flowfield to compute.

For the flat-plate inlet at the TUSQ tunnel conditions, the contribution to total absorption signal due to the freestream is approximately 1.5 times the size of the contribution of the shock layers as shown in Fig. 11(a). This can be contrasted with the conical inlet absorption signal shown in Fig. 11(b),

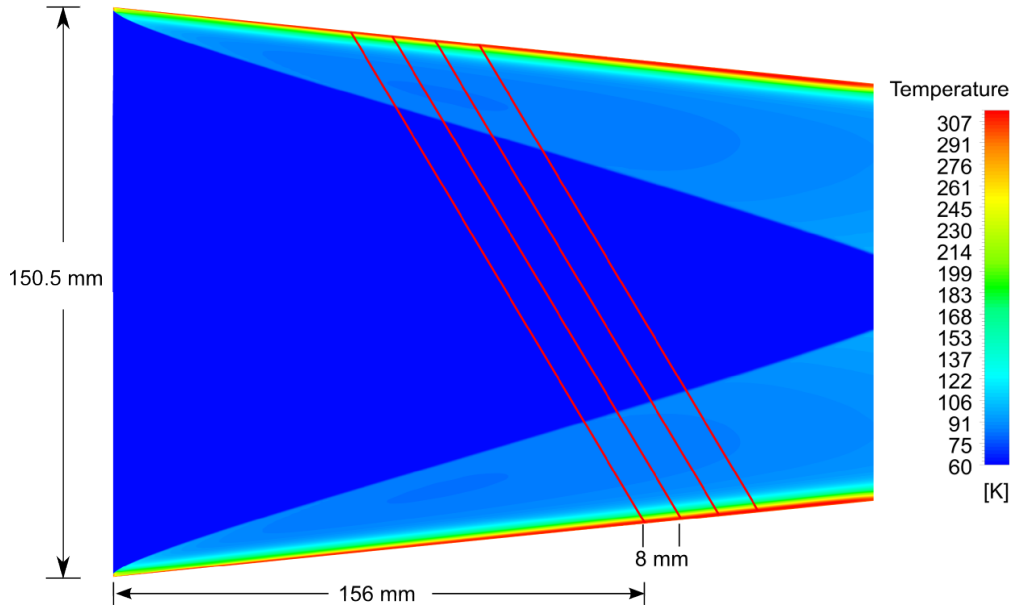

Figure 10: CFD temperature map for the conical inlet. Red lines indicate laser beam paths

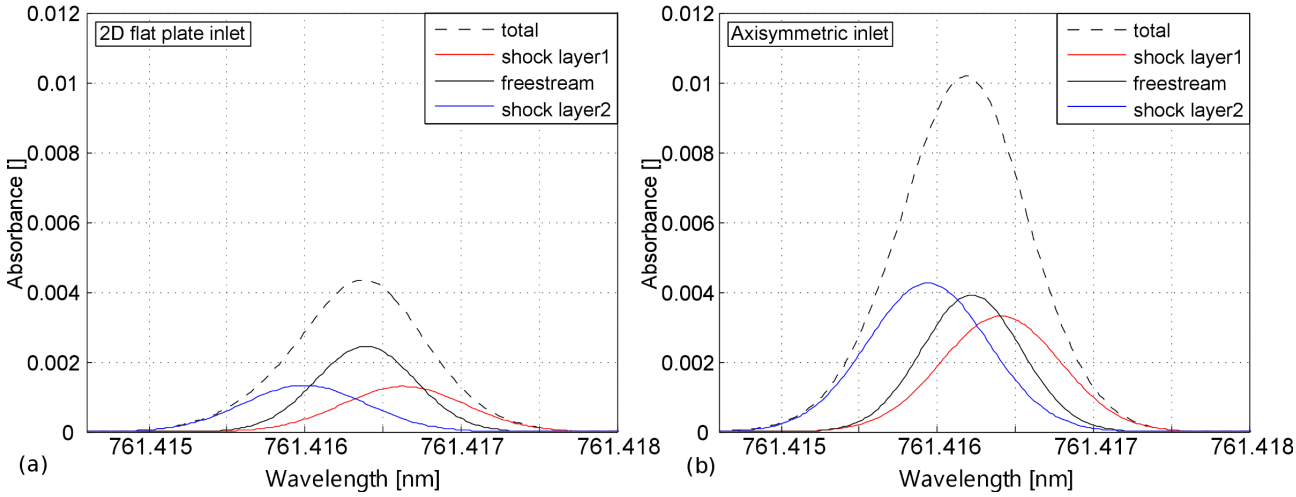

Figure 11: Comparison of the absorbance along the laser beam path for the (a) flat-plate and (b) conical inlet configurations at the TUSQ flow conditions

where the freestream contribution is smaller than that of the second shock layer. Comparison of the temperature maps in Figs. 8 and 10 shows that the conical inlet flow contains a larger fraction of the flow along the beam path within the shock layers than the flat-plate inlet flow.

It should also be noted, when comparing the two plots in Fig. 11(a), that the the 13 % longer path length caused by the use of the larger retroreflector provides 2.3 × larger total absorption signal for the conical inlet compared to the flat-plate inlet at the TUSQ tunnel conditions.

For the projected SCRAMSPACE flight conditions at an altitude of 30 km, u=2440 m/s p=1200 Pa, T=226.5 K and a Mach number of 8.1, the contributions to the absorbance signal for the conical inlet are shown in Fig. 12. Due to the higher freestream temperature, which increases from 65 K to 226.5 K, the resulting total absorbance signal is about 10 times weaker than for the tunnel conditions. The contribution of the freestream absorption to the total absorption signal is 4 times larger than the contribution of the shock layers. Comparing the results of Fig. 11 with those of Fig. 12, the

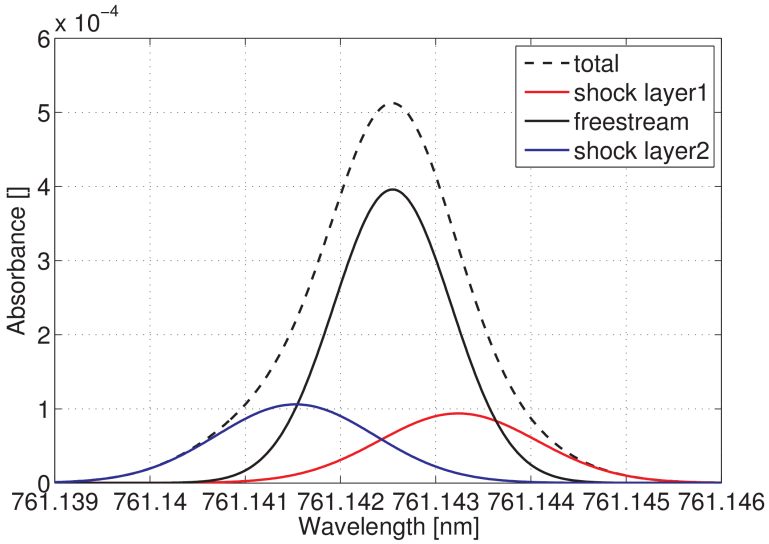

Figure 12: Absorbance in the shock layers and the freestream for the conical inlet at 30 km altitude, Mach 5.8 flight conditions

arrangement would be even more sensitive to the freestream conditions at flight conditions than it was for the facility tests in this report, and therefore less sensitive to the angle of attack, the effect of which mostly manifests through changes in the signal for the two shock layers. Note that for each of the two flow conditions, the absorbances presented in Figs. 11 and 12, the highest-signal transition in the R branch was chosen, to maximize the signal. This is a different transition for each of the two freestream conditions.

Despite the much lower signal at the freestream conditions, the peak absorbance of 5×10^{-4} for the conical should still be able to be measured by the log-ratio detector, provided other noise sources were not large. Thus, while it is an extremely challenging experiment, it is feasible to measure absorption in flight at an altitude of 30 km or lower.

5 Further Flat-Plate Inlet Results

The absorption measurements for the flat-plate inlet configuration were published in O'Byrne (2010). Since these results were published, further flow characterization experiments have been performed in the TUSQ facility, including total temperature and pitot pressure measurements presented in Sec. 2. This section presents comparisons between velocities and temperatures inferred from those measurements and the velocities and temperatures measured in the absorption experiments.

The short test time in pulsed hypersonic facilities like the one used in these experiments normally leads to the assumption of isentropic and adiabatic conditions. Figure 13(a) shows the results of a pitot study carried out in the facility (Buttsworth et al. 2011), revealing that the Mach number deviates from the initial nozzle design target of Mach 6. It starts at Mach 5.8 and drops during the 0.2-second test time to Mach 5.7. CFD calculations confirm that this effect can be attributed to a growing boundary layer inside the nozzle during the flow time.

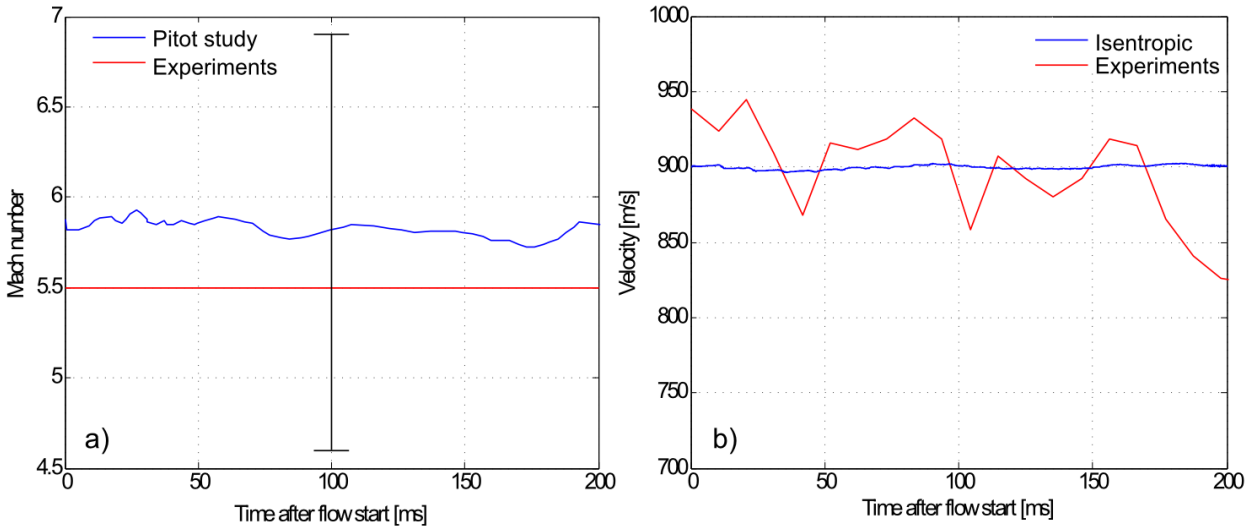

Figure 13: Comparison of Mach number and velocity measurements using the optical sensor with a pitot-based measurement

In combination with the measured stagnation pressure the velocity development at the nozzle exit using an isentropic expansion but otherwise assuming adiabatic conditions was calculated. In Fig. 13(b), the results are compared with the measured velocity from the laser-based arrangement. Assuming adiabatic conditions the velocity would drop by less than 2 m/s during the test time, whereas the laser-based measurements indicated a much larger decrease of 113 m/s over that time.

The laser-based measurements suggest a consistent decline in both velocity and temperature during the test time. As mentioned above, this effect can't be fully attributed to a growing boundary layer and the resulting drop in Mach number as the CFD calculations combined with the pitot measurements show.

As outlined in Sec. 2, recent experiments have been performed at TUSQ to measure the stagnation temperature history of the facility, using a thermocouple probe with a heated shield positioned in the freestream of the flow Buttsworth and Smart (2010). Using the Mach number from the pitot pressure study Buttsworth et al. (2011) the freestream temperature T_∞ can be calculated using (Anderson 1990)

$$\frac{T_0}{T} = 1 + \frac{\gamma - 1}{2} M^2 \tag{1}$$

Figure 2 shows the time history of the stagnation temperature, which drops during the test time from 720 K down to 256 K, with the bulk of the drop occurring for $t > 160$ ms after flow initiation. Figure 14 shows the resulting freestream temperature based on the Mach number and stagnation temperature using Eq. 1 and the measured freestream temperature from the present experiments. Both measurements show agreement within 10 K for the first 160 ms. After 160 ms the freestream temperature based on Mach number and stagnation temperature rapidly drops by 30 K.

Oxygen starts to liquefy for temperatures below 55 K, which may explain the relative stability of the freestream temperature measured using the diode laser sensor during the steep decline in the

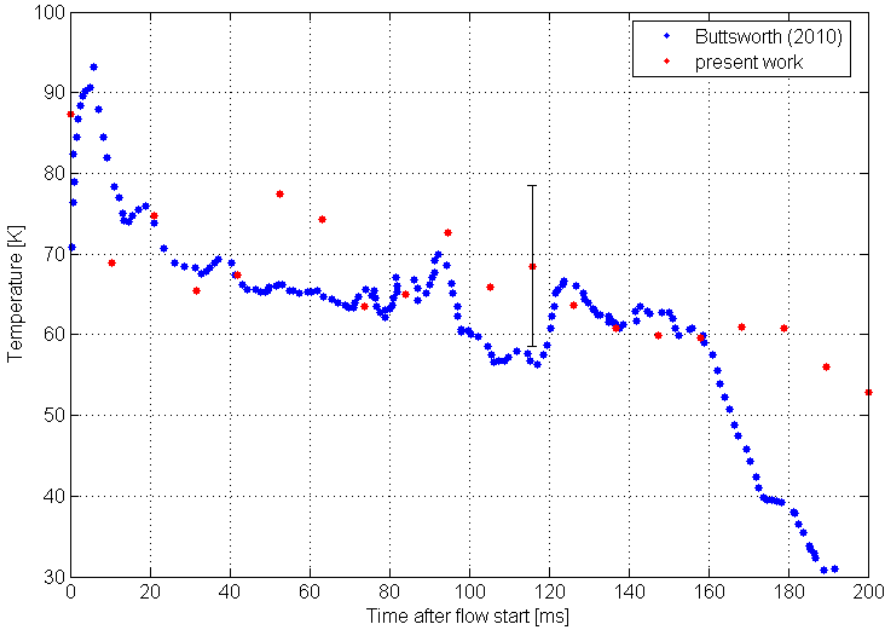

Figure 14: Comparison of measured freestream temperature with the computations of Buttsworth (2010)

measured stagnation temperature. Excluding measurements beyond 160 ms after flow initiaion, the mean freestream temperature derived from the present experiments is 67.6 K compared to 66.5 K for the stagnation temperature and pitot pressure measurements, which constitutes consistent agreement between the two techniques.

Both measurements confirm that the temperature actually drops during the test time. Therefore the adiabatic assumption is not correct and energy transfer over the system's boundaries have to be considered. As stated previously, this is most likely caused by conductive heat loss to the nozzle walls. To confirm this, further investigations including a time-dependent CFD-thermal simulation of the nozzle flow would be required.

Compared with conventional systems such as pitot rakes, the non-intrusive diode-laser-based sensor can monitor the flow freestream velocity and static temperature of the flow without disturbing it, and can therefore be used in conjunction with other experimental arrangements in a nozzle flow. As it makes independent direct measurements of temperature and velocity, it accounts for both thermal and kinetic effects on the Mach number, unlike Mach number determination by pitot pressure measurements.

Figure 15 plots the nozzle reservoir pressure and the diode laser velocity measurements on the same time scale. The fluctuations in the velocity measurement correlate well with the fluctuations in the measured nozzle reservoir pressure. Once again, the two plots diverge at around 160 ms after the start time, with the reservoir pressure continuing to decrease. Comparing the diode laser velocity measurements with the velocity measured using the pitot pressure measurements in Fig. 13(b) shows that the pitot measurement is not as sensitive to the velocity fluctuations as the diode laser sensor.

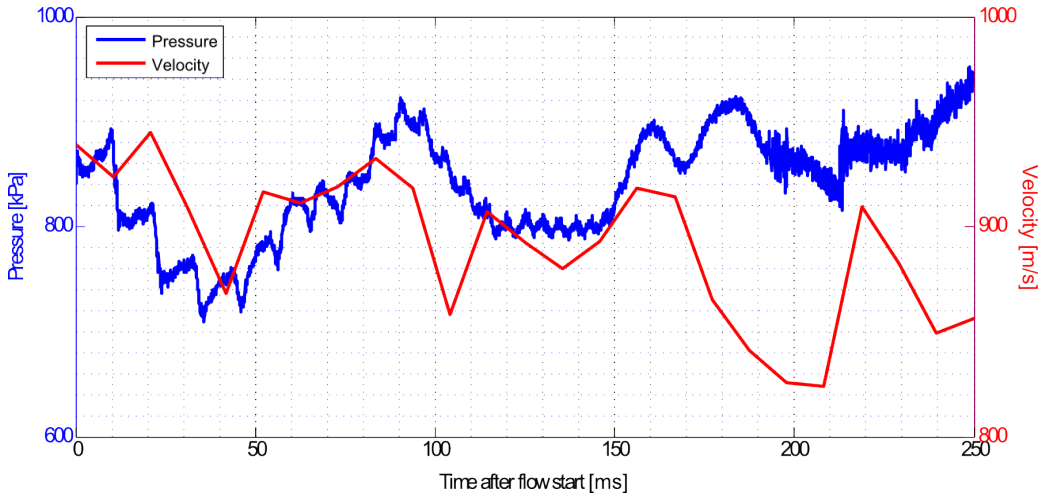

Figure 15: Nozzle reservoir pressure and velocity plots

5.1 Effect of Noise on Measurements

Fitting the theoretical to the experimental data for a noise-free spectrum is straightforward, but noise will limit the sensitivity of this technique. Noise sources include mechanical vibrations, time-varying etalons resulting from the interference from the optical components, electronic noise, stray light sources and — for high-enthalpy hypersonic flows like those in shock tunnels — flow luminosity.

To investigate the effect of amplitude noise on the measurement uncertainty an artificial signal was generated by adding high-frequency Gaussian noise with an average relative value compared with the largest peak absorbance of between 0 and 175 % to a computed absorption signal for a flow matching the expected tunnel freestream conditions detailed in Sec. 2. The particular type of Gaussian noise was chosen based on an analysis of the noise present between peaks in pre-flow experimental data. Figure 16 shows the histogram for the observed noise.

For each noise level, 100 different spectra for velocities in the range 800–1000 m/s and temperatures in the range 30–50 K were generated. The fitting routine was then used to either match the velocity or the temperature to the non-fitted value assumed known, starting from different randomized initial guesses.

Even where the noise is as large as the signal, the routine was able to fit to the velocity well. The fit is so good even in the presence of noise because of the accuracy of the freestream Doppler shift measurement: The retroreflector guarantees that the beam returns at the same angle it entered with, so that the separation between the two transitions is a function only of the Doppler shift and does not depend on measurement of some external reference velocity. The noise has minimal effect on the velocity prediction because this depends on the location of the shifted peaks rather than their amplitude and the peak location is much less sensitive to amplitude noise than the peak amplitude.

The results of these tests are summarized in Fig. 17 as linear fits to the data. It is clear from this plot that the systematic errors in velocity and temperature vary linearly with the noise amplitude. For the velocity fit even for spectra with noise up to 150 % of the signal amplitude a standard deviation within ± 4 % was observed during this simulation. This shows the robustness of the velocity fit in the

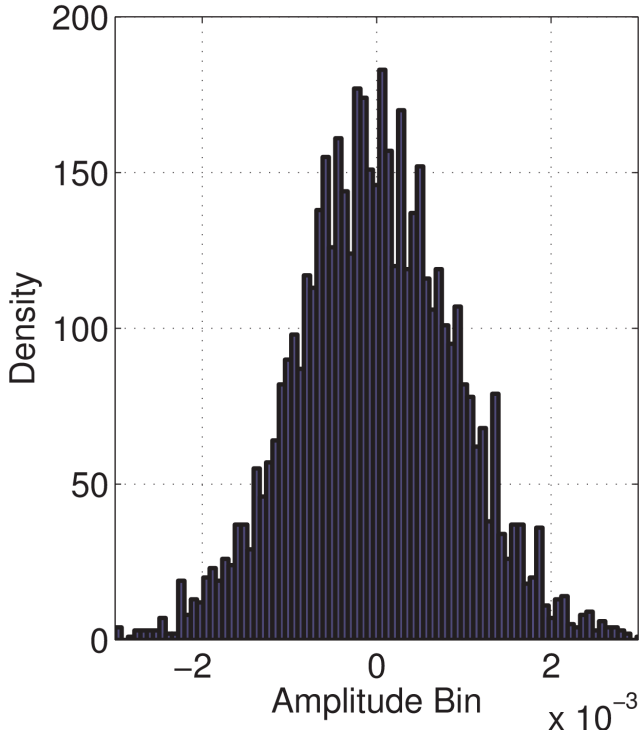

Figure 16: Noise histogram for experimental absorption data

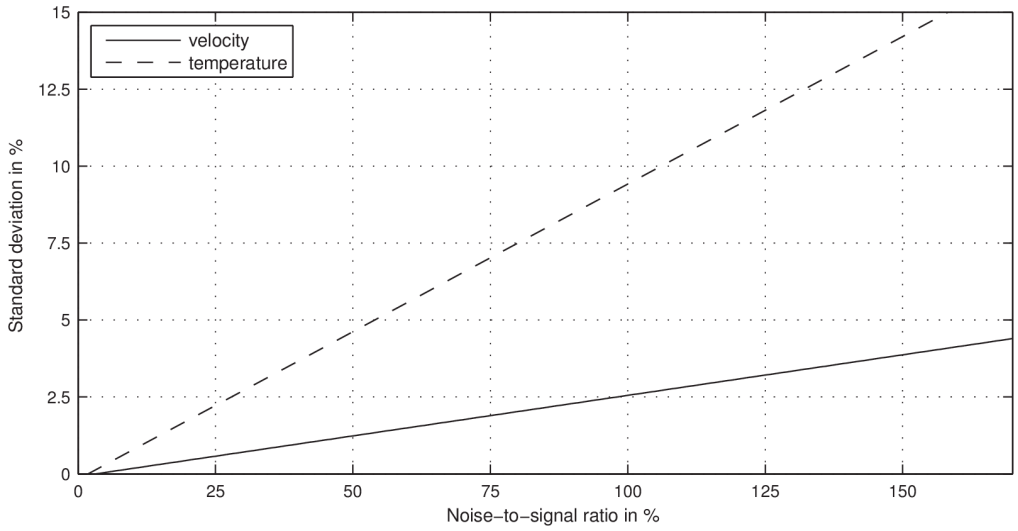

Figure 17: Plot showing the effect of noise on temperature and velocity measurements

routine. With a standard deviation of over $\pm$ 13 % at 150 % added noise, the temperature fits are much more sensitive to noise, as the fitting routine requires at least two or more peaks and relies on their amplitude ratio. In realiistic field measurements, even higher standard deviations for the temperature measurements are expected, as additional low-frequency disturbances can randomly shift the baseline of the spectrum. The baseline shift has little effect on the velocity measurement, which relies on the frequency spacing between the peaks rather than the amplitudes of those peaks.

High-frequency noise will have less effect than frequencies similar to those of the spectral lines. At faster scan rates mechanical noise would only manifest as a DC offset, which is easier to correct for.

5.2 Effect of Offset on Temperature Measurements

The temperature measurements obtained for the flat plate condition had a standard deviation of approximately 20 K, based upon scan-to-scan variations within a single tunnel run. Part of the reason for this relatively high temperature scatter is that the signal itself was noisy. In addition, the time-scales of the noise and the absorption peaks could be quite similar. Another reason for possible increased uncertainty in the temperature measurement is a failure to adequately subtract the background from the spectrum. This problem can be significant if the dominant periods of the noise are similar to the scan times of the spectra. In this case, fitting a low-order polynomial to the background may not be effective.

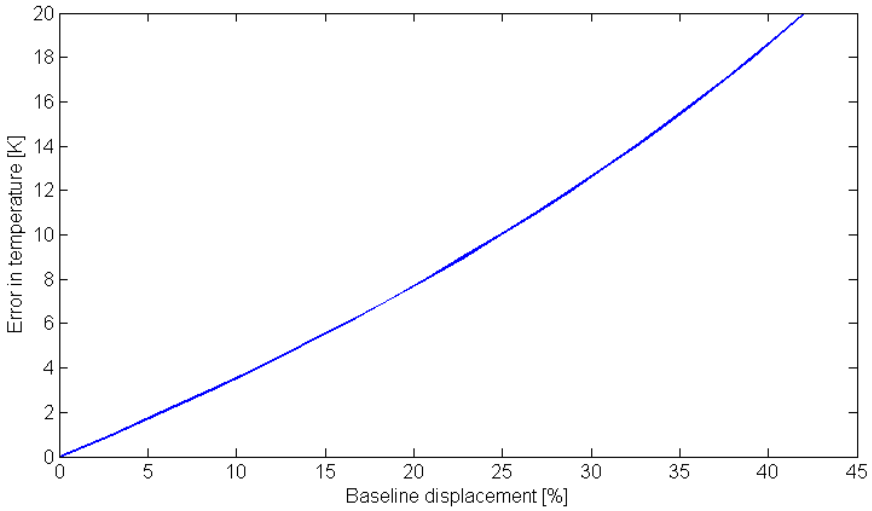

Figure 18: Plot showing the effect of an offset on the measured temperature

In order to determine the effect of incorrect offset subtraction on the measured temperature, spectra were simulated for the conical inlet configuration and non-zero offsets were added to the spectra before the temperature was fitted. The results are presented in Fig. 18. This analysis gives an indication of how the systematic error in a temperature measurement can be influenced by the quality of a background fit, but only considers cases where all absorption peaks experience the same offset. In general, a poor background fit implies that different peaks will have different offsets. In Fig. 18, the baseline displacement on the x-axis is expressed as a percentage of the peak height. Thus, a baseline offset of 20% of the peak height would result in a systematic temperature error of 8 K over the tuning range of the VCSEL between 760.5 and 761.5 nm.

6 Conical Inlet Facility Tests

6.1 Unstart

For the first tunnel runs with the conical inlet model, no Doppler-shifted peaks were visible in the recorded data. A Schlieren recording revealed that the inlet choked during the test time, forming a

bow shock in front of the inlet, with subsonic flow downstream of that shock. Figure 19 shows a series of five pictures showing a normal shock in front of the inlet. The time between individual pictures was 0.2 ms, and Fig. 19 shows the flow at a selection of these times during what would normally be the starting time for the hypersonic flow.

The images in Fig. 19 indicate that the flow is initially hypersonic inside the nozzle, with an oblique shock clearly visible at the top of the image at $t = 4\,\text{ms}$. By $t = 5\,\text{ms}$, however, a normal shock appears outside the inlet and propagates upstream for the remainder of the flow time.

The manufacturing of the inlet on the lathe produced an exit diameter of 87.3 mm on the conical nozzle which was smaller than originally planned 95.8 mm exit diameter. An additional 2 mm forward-facing step left over from the manufacturing process reduced the area to below the area ratio required for the successful starting of the inlet flow.

The isentropic relation between the inlet and the throat area determines the physical limit for a started inlet at a given Mach number. But especially for conical inlets, a throat area above the required A^* does not guarantee successful starting of the inlet. Kantrowitz and Donaldson (1945) developed a criterion which describes the maximum aerodynamic contraction ratio for an isentropic gas for which successful starting of the hypersonic flow is guaranteed:

$$\frac{A_t}{A_i} = \sqrt{\frac{\frac{2}{\gamma-1} + M_\infty^2}{\frac{2}{\gamma-1}\gamma M_\infty^2 - 1}}_2 \left[\frac{1 + \frac{\gamma-1}{2}M_\infty^2}{1 + \frac{\gamma-1}{2}}\right]^{-\frac{1}{2}\frac{\gamma+1}{\gamma-1}} \tag{2}$$

where A_t is the throat area, A_i is the inlet area and M_∞ is the freestream Mach number. This criterion is determined by assuming a normal shock wave at the inlet and expanding the post-shock flow to the sonic point inside the nozzle. Inlet starting between the Kantrowitz and isentropic limits is still possible but depends strongly on the actual flow conditions, the inlet geometry and the flow establishment process. The pressure ratio between the incoming freestream flow and the ambient pressure in the test section before flow arrival also plays an important role.

Experimental results with a scramjet inlet conducted in an arc heated test facility (Smart 2001) showed that successful inlet starts below the Kantrowitz limit are possible. In a numerical study featuring several inlet and flow configurations Tahir et al. (2003) demonstrated using computations that a successful start is possible, especially in impulse facilities. The large pressure gradients help to establish a supersonic flow field.

Figure 20 shows a graph plotting area ratio over freestream Mach number including the isentropic limit and the Kantrowitz criterion. Successful inlet starts by Tahir and Smart are highlighted. The upwards pointing solid triangle in Fig. 20 indicates the area ratio and freestream Mach number for the unstarted flow.

Using this analysis the inlet was modified by cutting off part of the back of the inlet upstream of the original exit location, as shown in Fig. 21. The two triangles in Fig. 20 depict the conical model's area ratio before and after the modification. While still below the Kantrowitz line, the modified inlet has

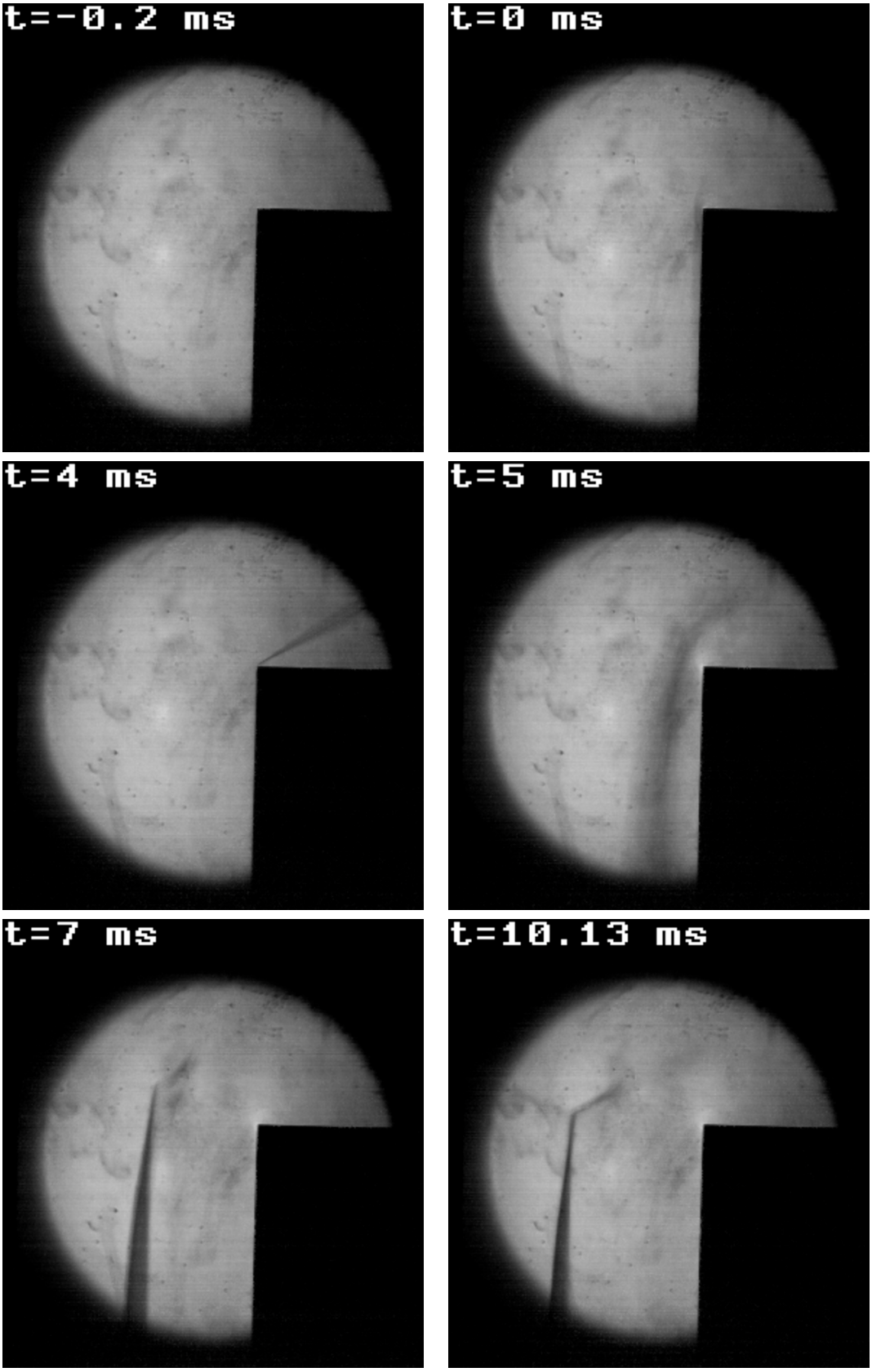

Figure 19: Schlieren images for nonstarting inlet

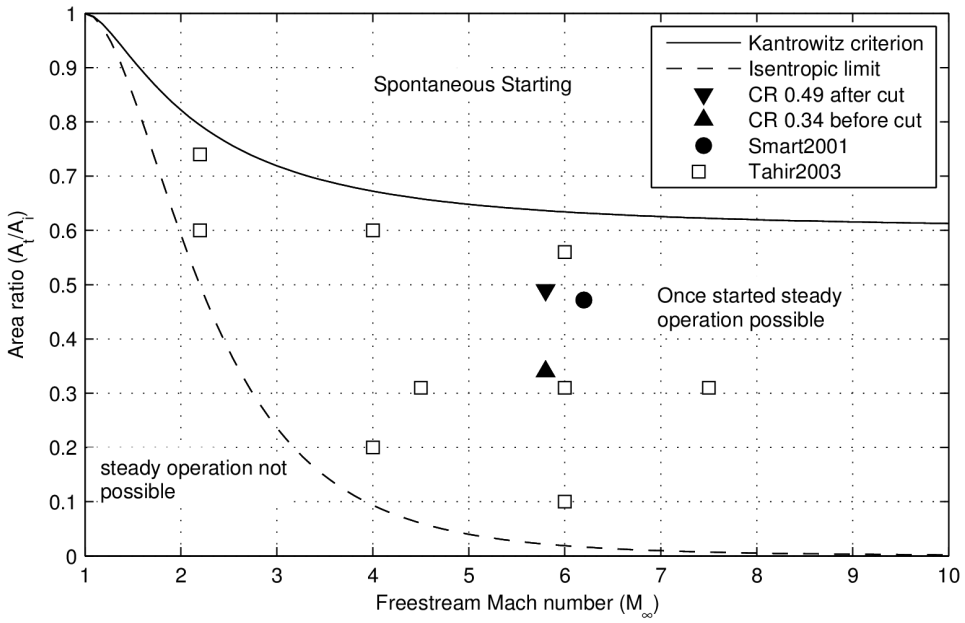

Figure 20: Plot showing regions of self-starting flow in a conical inlet at hypersonic speed

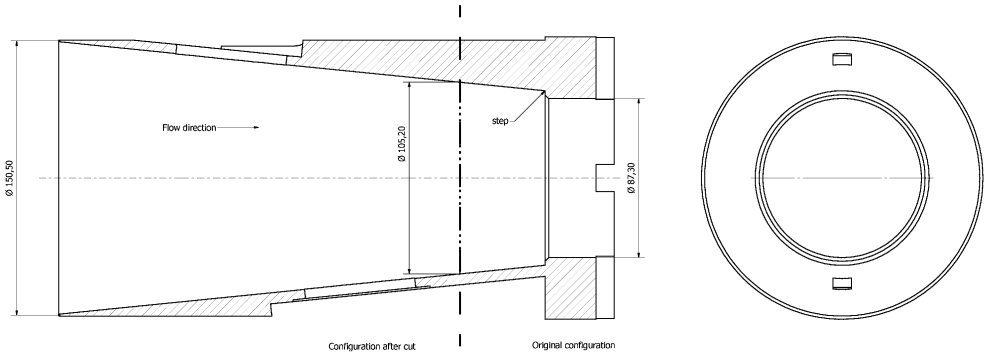

Figure 21: Diagram of conical inlet showing region cut of to prevent choked flow

an area ratio which brings it much closer to that line. van Wie (2000) suggests that the Kantrowitz criterion's assumption of a single normal shock is a conservative estimate at higher Mach numbers.

Figure 22 shows Schlieren recordings from the modified inlet during a tunnel run. At 1.4 ms after flow initiation the leading edge shock at the upper edge of the inlet is visible. Disturbances behind the shock resulting from the upper reflector box are visible but do not result in flow spillage from this area into the inlet. At 6 ms a shock originating from the left side appears. The shock angle is inclined 23.8° towards the flow. It is apparent in some of the pictures at later times that there is a shock wave entering the inlet and originating from the nozzle. This may be due to an over-expansion of the nozzle flow, as the 500-Pa nozzle exit pressure is similar to and for some tunnel runs lower than the test section pressure, which could reach as high as 1000 Pa for some tunnel runs.

Figure 23 shows a comparison between absorption spectra for an unstarted (top) and a started (bottom) inlet. Due to experimental constraints two different absorption lines had to be chosen. The spectra are shown as plots of wavelength vs time, with the color of each point corresponding to the absorbance

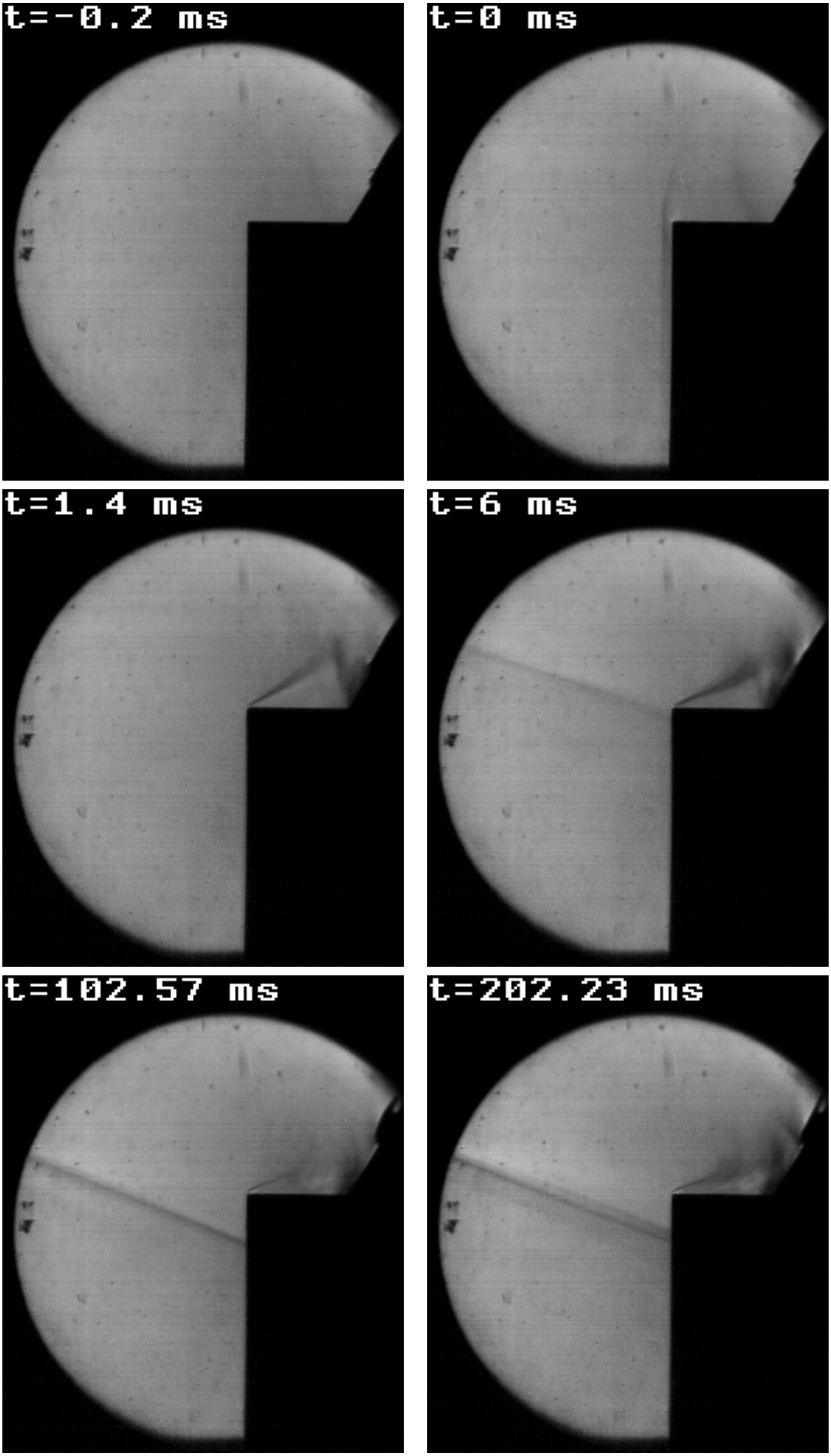

Figure 22: Schlieren images for started inlet

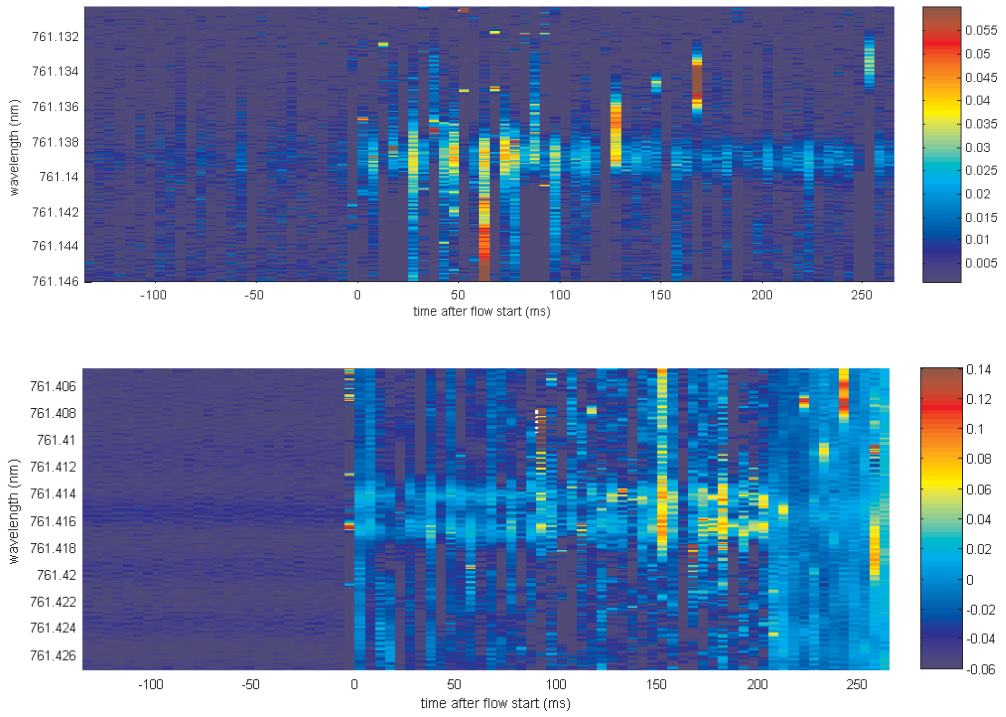

Figure 23: Comparison between absorption spectra for an unstarted (upper image) and a started (lower image) inlet

at that wavelength.

The unstarted inlet spectra at the top of Fig. 23 show the two Doppler-shifted peaks overlapping, forming a single broad peak. This results from the low subsonic flow velocity behind the separated shock wave and broadening due to the high post-shock pressure in the unstarted nozzle. The higher absorption level compared to the pre- and post-flow levels can also be explained by the higher pressure of the freestream. Assuming isentropic conditions the inlet conditions change from M=5.8, p_0=660 Pa, T_0=55 K upstream of the normal shock to M_1=0.4, T_1=411 K and p_1=26 kPa downstream of the normal shock. The higher temperature reduces the absorption signal but this effect is outweighed by the much higher pressure which increases the absorption. The higher pressure by itself would increase the absorbance by a factor of 22.4 whereas the higher temperature decreases the absorbance by only 2.6, resulting in a net increase of absorption signal by a factor of 8.6 for the unstarted condition.

The spectra in the lower part of Fig. 23 show the absorbance for the case where the hypersonic flow is allowed to start, after the model modification. The splitting of the two peaks is quite apparent in the figure, from the time the flow starts until just after 200 ms after flow initiation, when the two peaks begin to merge once again as the flow slows down. Although the signal-to-noise ratio of the absorbance signal was not as high as for the flat-plate data, Fig. 23 shows that it is very straightforward to detect the presence of unstart in the inlet with this sensor.

6.2 Velocity Measurements

The initial problems with inlet starting and oscillation problems with the log-ratio circuit only allowed the detection system to scan over two lines (R3Q4 and R3R3)of the oxygen A band. Because several of the available tunnel runs were used to ensure that the conical inlet flow started, only two tunnel runs were available for acquiring hypersonic data. Mechanical problems with the laser diode mount made it necessary to permanently mount the diode in the mounting tube. As a result the total laser beam intensity was no longer adjustable by changing the angular position of the laser diode. This resulted in a saturation of the input channels of the detector for scans over more than two spectral lines. A mechanical redesign of the laser mount should remedy this issue and allow to scan over more than two lines.

Because there were only 1 or 2 lines measured in each spectrum for the conical inlet tests, it was possible to measure a freestream velocity based upon the measured Doppler shift of the transition, although it was not possible to measure a temperature for these tests. Velocity was calculated in the same manner as for the flat-plate inlet, and the method is explained in detail in O'Byrne (2010) and Wittig and O'Byrne (2011). An offset signal was subtracted from each spectrum and Gaussian absorbance distributions were fitted to each of the two measured peaks. Figure 24 shows one such fit for one of the transitions at the conical inlet condition.

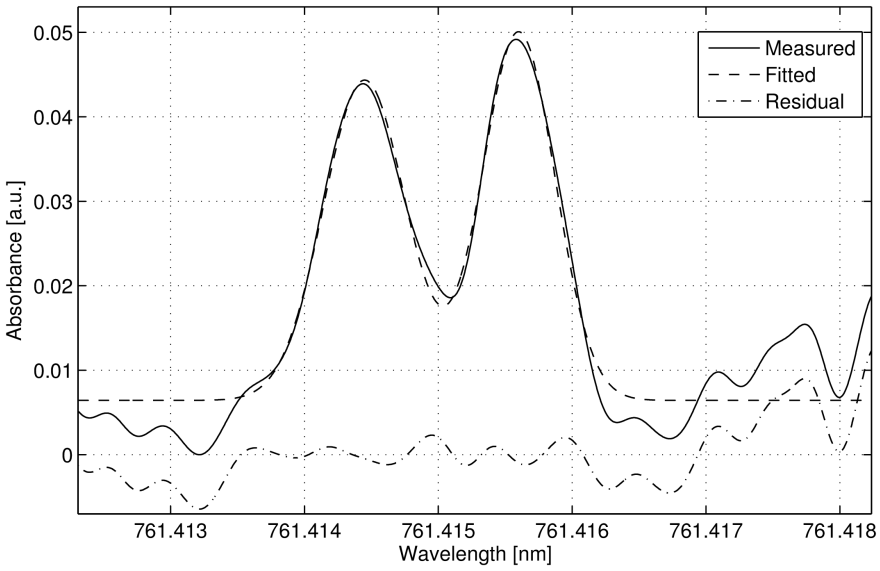

Figure 24: Fit to Doppler-shifted peaks for conical inlet configuration

The different geometry of the conical inlet results in a different absorbance signal compared to the flat-plat inlet absorbance. Figure 10 shows a CFD calculation of the conical inlet flow field with laser beam path marked in red. The smaller angle of 7.2° for the conical inlet compared with 10° for flat-plate inlet results in a 10 K lower temperature in the shock layer region of the conical inlet.

The velocities for two tunnel runs where the inlet remained hypersonic were obtained, and are presented in Fig. 25. Included in this figure is the velocity measurement obtained using the flat-plate inlet,

for comparison. Each of the two plots was obtained using a single transition, to make the comparison between the two measurements more fair.

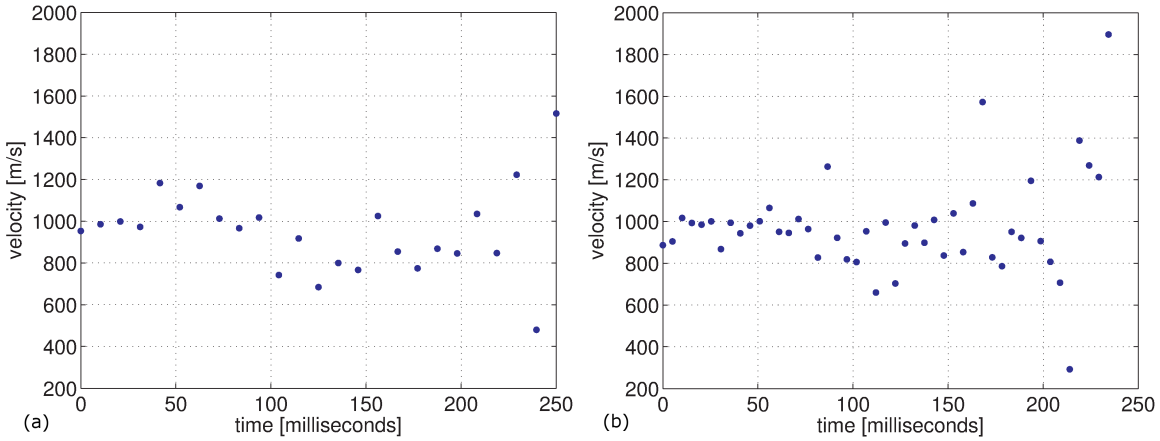

Figure 25: Comparison of freestream velocity calculated using (a) flat-plate and (b) conical inlet configurations

The average velocity over all data points during the flow time is 962 m/s for the conical inlet, which is higher than 900 m/s measured during the previous campaign using the flat-plate inlet, but the overlap between the two measurements is within the measurement uncertainty of $\pm$40 m/s. It also has to be considered, that for the axisymmetric experiments fewer data points (a total of 120) were available, compared with the 640 measurements used in the flat-plate inlet experiments. An investigation of the stagnation pressure recordings and other parameters related to the operation of the tunnel did not reveal any significant differences between the two experimental campaigns.

Both plots show similar trends with time, although the scatter is noticeably greater for the conical inlet configuration. Both measurements also show a similar increase in the measurement scatter after 200 ms, which correlates well with the measured changes in the other flow properties mentioned previously.

Figure 25 shows that for a single absorption line the measured velocity has a standard deviation of 110 m/s for the 2D inlet and 130 m/s for the axisymmetric inlet. These values are similar, despite the lower signal-to-noise ratio (SNR) of 2 to 1 for the axisymmetric inlet compared with 5 to 1 for the flat plate inlet. This increase of 2 % relative to the mean velocity generally concurs with the observations regarding the influence of noise made in Sec. 5.1, which state that a decrease in SNR by a factor 2.5 would only result in a modest increase in standard deviation of 1 % for purely Gaussian noise.

7 Wavelength Modulation

7.1 Wavelength Modulation Tests in Ambient Air

While the log-ratio amplification system used for all the tunnel tests in this report was electronically very simple and reasonably robust, it has two major drawbacks in its current form: the scan rate is

limited to a maximum 100–150 spectra per second because of the bandwidth of the detector, and the optical system requires both a signal beam and a reference beam to measured the absorbance. The scan rate of the log-ratio detector is fast enough for a flight test in terms of acquiring data, but it is slow enough for the absorption signal to have signal components at frequencies where the effect of mechanical vibrations have the most effect on the optical signal. A scan rate around 10 kHz would place the signal at a higher frequency than the noise due to vibration, resulting in a less noisy absorption signal, and this bandwidth is achievable with the wavelength modulation detection system.

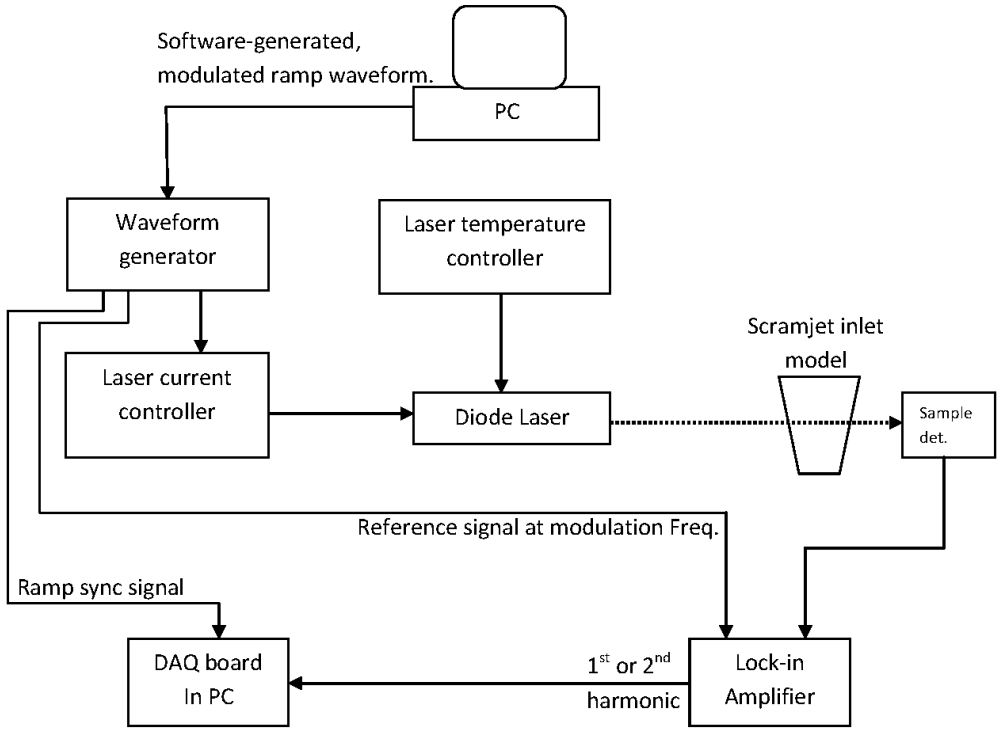

Figure 26: Arrangement for wavelength modulation experiments

In order to test the wavelength modulation technique, experiments were performed on the conical inlet model at ambient conditions. The experimental arrangement for these tests is shown in Fig. 26. Measurements were performed using the inlet model and optical system, with the same laser diode, current controller and temperature controller used as for the TUSQ conical inlet tests. The system was set up for six passes through the inlet, providing a total path length of 0.84 m for the test.

A sinusoidal modulation signal was generated by the Agilent signal generator, with an amplitude of 16.7 mV p-p and frequency of 30 kHz. This sinusoidal signal was superimposed upon a ramp voltage with an amplitude of 500 mV and an offset of 850 mV. This was used to drive the laser. A Signal Recovery Model 7280 DSP-based lock-in amplifier was used to acquire the lock-in signal, and was synchronized to the sinusoidal modulation frequency. A single 10 mm$\times$10 mm silicon PIN photodiode was used as the input to the lock-in amplifier. The reference photodiode in the conical inlet model was not used for these measurements.

Data was acquired with a National Instruments PCI6115E data acquisition card asynchronously sam-

Variable	Value
Ramp sweep frequency	100 Hz
Modulation frequency	30 kHz
Wavelength/current rate	0.28nm/mA
Ramp amplitude	500 mV (2.5 mA)
Ramp offset	850 mV (4.25 mA)
Wavelength range of scan	0.7 nm
Modulation depth	16.7 mV p-p or 0.083 mA p-p
Modulation depth (in terms of laser wavelength)	0.023 nm

Table 4: Signal settings for wavelength modulation tests

pling the spectral signal and the current ramp synchronization signal at 100 ksamples/sec, yielding 1000 points (± 1) per spectral scan. Data was taken for 1.28 sec, resulting in 128 scans.

The important parameters used in the test are summarized in Tab. 4. The modulation frequency chosen was low enough to be considered wavelength modulation rather than frequency modulation (Silver 1992). The modulation index was approximately 7.7 for these measurements, based upon the calculated transition half-width of 0.0031 nm.

The Model 7280 lock-in can detect at either the modulation frequency (1f detection) or twice the modulation frequency (2f detection). Fig. 27 shows single-acquisition scans for the two detection methods. The gray horizontal lines indicate three times the standard deviation (3σ) for the 128 spectra measured. Each of the plots is of a representative single spectrum over the 0.7-nm tuning range of the VCSEL.

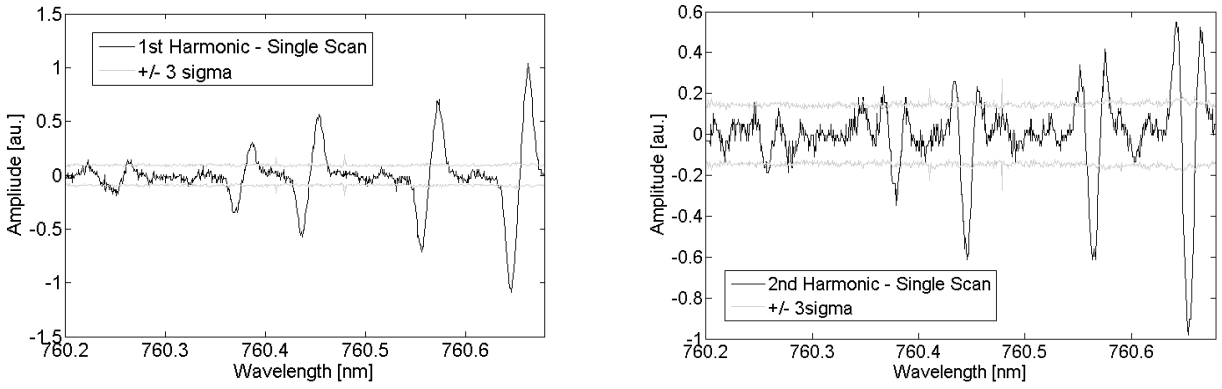

(a) (b)

Figure 27: Wavelength modulation signals showing 3σ lines for both (a) 1f and (b) 2f wavelength modulation detection

The spectra in Fig. 27 show the expected shapes for first- and second-derivative wavelength modulation spectra. For the first-derivative spectrum in Fig. 27(a), the signal-to-noise ratio of the largest of the spectral lines is approximately 10, reducing to approximately 2 for the lowest-wavelength transition. The absorption signal at flight conditions is approximately 12 times smaller than the measured signal at standard temperature and pressure. Because the absorption signal is split by the Doppler shift at the high Mach number conditions in flight, this peak absorbance is further reduced by a factor

of two. Thus, even for the largest of the transitions, the SNR would be less than 1. For the second-derivative spectrum, the SNR varies from 2 to 7, depending on the transition. For both 1f and 2f spectra, this is considerably worse than the SNR of 40 achievable on a single scan with the log-ratio amplifier. Averaging over several spectra can help, but this would reduce the time resolution of the detection system, one of its major advantages.

Other authors have claimed much better sensitivities than those produced here, so the system needs to be better optimized before it can be discounted entirely. In particular, the system needs to be tested for the lower modulation index recommended by Silver (1992). As mentioned above, one significant advantage of the 2f detection system over the current detector is that spectra can be scanned at higher frequencies than the log102 detector used for the inlet experiments in this study. Scan rates of several kHz were achieved in this configuration with no significant loss of signal. As the vibration frequencies expected to be experienced by the measurement system are in the low kHz range and below, detection at higher frequencies combined with high-pass filtering has the potential to significantly reduce the effect of vibration on the measurement quality.

7.2 Lock-in Amplifier Design

While the wavelength modulation detection system in Sec. 7.1 is very flexible and composed of high-quality commercial units, the components are too large to be used in a flight test. During this project we designed and built a prototype lock-in amplifier circuit for testing with the TDLAS system, with a view to further miniaturizing the system for flight in future iterations of the design. The details of the foils and circuit diagram for the design are contained in Appendix F of the report.

The arrangement of the circuit is shown in Fig. 28. The circuit consist of a power supply board and the following components:

- Input stage
- Bandpass filter
- Reference input
- Phase detector
- Output filter/amplifier

The input stage consists of photodiode preamplifier, a ramp signal preamplifier and an amplifier/ramp subtracter circuit. The photodiode preamplifier provides a 50 Ω load for the photodiode current and a conventional wide bandwidth, low-noise, low offset linear voltage amplifier. The nominal maximum voltage gain of this stage is 30 dB and can be adjusted by a potentiometer, as can the voltage offset. The ramp amplifier is much the same as the photodiode amplifier, but does not require the same gain. The ramp signal is intended to reflect the current ramp used the sweep the laser wavelength so that this can be removed from the photodiode signal prior to detection in the multiplier. The second gain

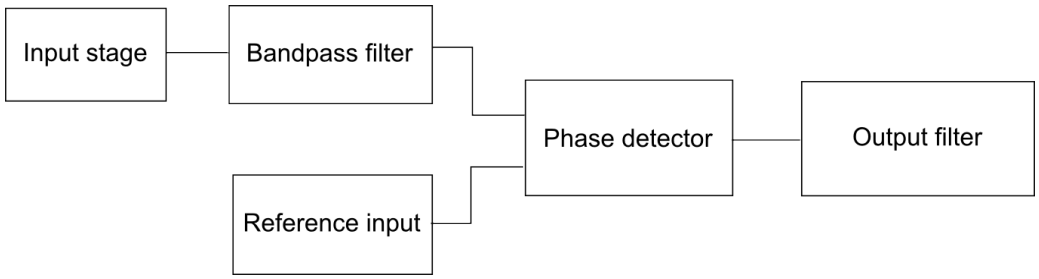

Figure 28: Block diagram for wavelength modulation detector

stage is a differential amplifier that provides an extra 30dB of gain to the photodiode signal and also subtracts the ramp component from the input signal.

The bandpass filter is employed to band-limit the undesirable noise components in the input signal prior to being mixed with the reference signal in the detector sub-circuit. It also provides extra gain to the input signal. It is based on a biquad bandpass design with independently variable gain, bandwidth and center frequency.

The reference input is derived from the same modulation signal that is superimposed on the laser current ramp. However, for 2f detection, the reference frequency must be twice the modulation frequency. This can be achieved by employing a dual channel function generator. For the lock-in amplifier to provide optimal detection, the 2f reference signal must be in phase with the 1f modulation signal.

The following two stages are unity gain phase shifters that provide variable phase shifts of up to 180° each.

The lock-in detector is based around an Analog Devices AD835 multiplier integrated circuit. A maximum voltage gain of 12 dB (x4) is available and controlled by potentiometers. An output frequency response in excess of 20 MHz is achievable, which is sufficient for laser scan rates in excess of 10 kHz.

The output low-pass filter comprises two cascaded 2-pole stages. The respective roll off frequencies are determined by variable resistors and capacitors. Links facilitate the selection of filter stages in the signal chain. The output amplifier has a maximum voltage gain of 9.5 dB. DC offset trimming is also available.

The prototype wavelength modulation detector was tested by generating a simulated absorption signal generated using an arbitrary function generator. The signal consisted of the sum of a ramp representing the intensity increase due to the current ramp of the laser, a set of five Gaussian lines representing oxygen A-band transitions and a Gaussian noise signal. The contributions and final input signal to the detector are shown in Fig. 29. The amplitude of the noise signal could be varied to determine the filtering capability of the detector in a controlled manner. The final waveform shown in this figure has a peak amplitude of 5 mV.

Figure 30 shows the signal as it progresses through the detector. Figure 30(a) shows the input signal, generated from the three constituent signals in Fig. 29, while Fig. 30(b) shows the signal after having been amplified, had the slope removed and filtered by the first two stages in Fig. 28. Figure 30(c) shows the 2f output of the detector. This output has a peak height of 1 V after amplification, and shows excellent signal-to-noise ratio compared with the original input signal.

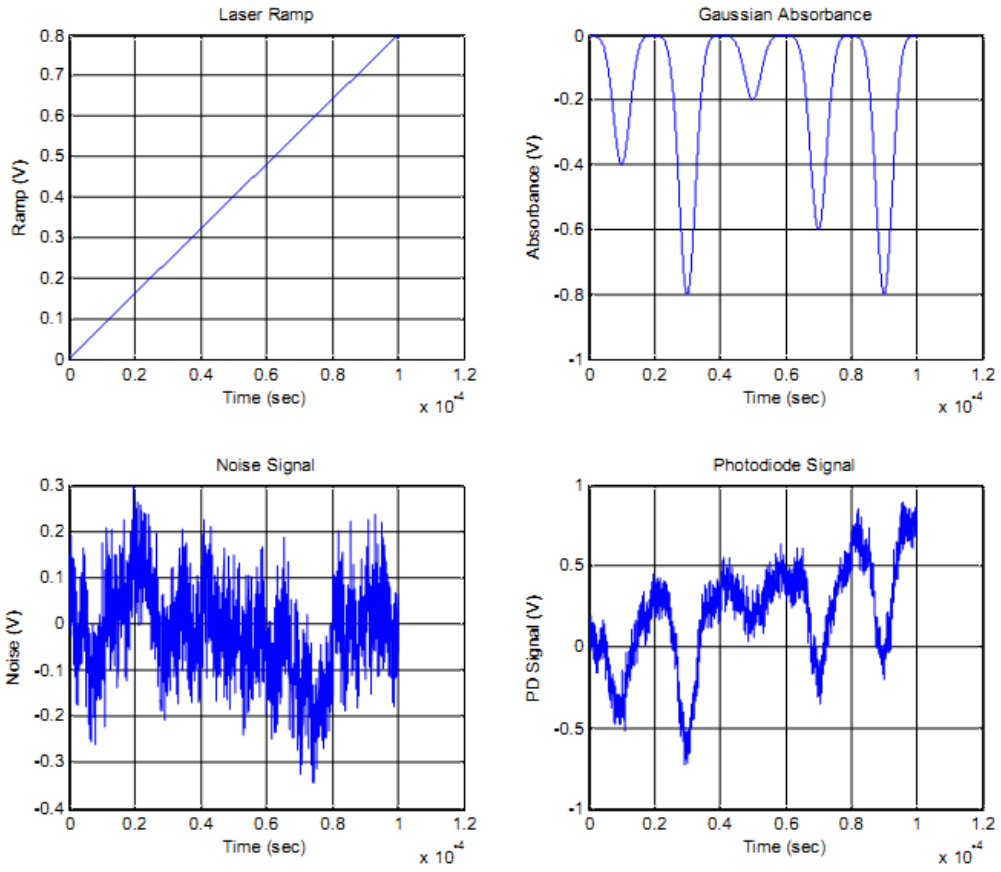

Figure 29: Generated input signal for prototype wavelength modulation detector testing

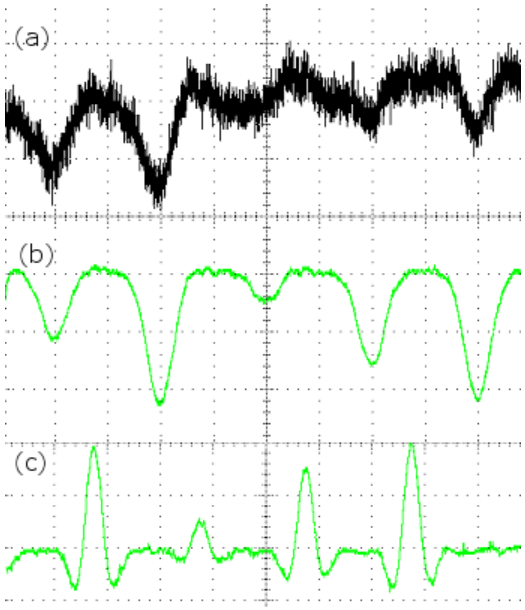

Figure 30: (a) Input signal, (b) signal filtered and offset removed (c) 2f wavelength modulation signal

In generating this output, careful attention had to be paid to removing offsets to the signal by tuning potentiometers. Offsets in the input signal would cause oscillations in the final 2f output signal. Provided these offsets can be removed during the test, this detector shows promise for precise measurements using real photocurrents.

8 Physical Response Tests

The results presented in O'Byrne (2010) and Wittig and O'Byrne (2011) showed significant noise on the signal. In O'Byrne (2010) two plausible explanations for this additional noise during the tunnel tests were presented: beam steering due to density variations along the laser path and mechanical vibrations in the model. In this section, experiments investigating both of these explanations are presented. The beam steering was tested by installing a laser system outside the tunnel to determine the displacement of the beam on a CCD array, and was computed using the predicted density distribution in the nozzle flow. For the conical nozzle tests, a new optical mounting system was designed to be more resistant to vibration, and vibration tests were performed to determine how successful the redesign was.

8.1 Beam Steering

The inlet, being either a rectangular converging or conical converging duct, generates shock waves which can refract light. In addition, turbulent variations in the nozzle flow can have the same effect. As the TUSQ facility is a relatively new hypersonic facility, the turbulence behavior of the facility is still not quantified, so that while the effects of the shock waves on beam steering can be calculated analytically, the turbulence effects must be investigated experimentally.

Beam steering, either by the shock waves in the inlet or by turbulence in the freestream, causes large variability in the log-ratio signal when its extent is large enough to cause the beam to be displaced by more than approximately 3 mm on the 10 mm by 10 mm detector, as this causes a reduction in the intensity ratio between the signal beam and the reference beam, because the path of the reference beam is not influenced by the beam steering.

During the conical inlet tests, one tunnel run was used to investigate the effect of possible beam steering due to turbulent variations on the absorption signal. The experimental arrangement for this test is shown in Fig. 31.

The light from a 650-nm diode laser pointer was directed through the test section windows and through the diameter of the nozzle flow, onto the Redlake high-speed camera, located approximately 1850 mm from the axis of the Mach 5.8 contoured nozzle. The camera had no lens, with the laser beam impinging directly onto the CCD. A neutral-density filter was used to attenuate the laser beam so that it did not saturate the detector. Both the laser and camera were mounted to the floor of the laboratory rather than to the test section, isolating the effect of the tunnel recoil from the measurement. Although the laser only passes through the test section once, any displacement in the path of the beam from the mean position before the run will be amplified over the distance between the nozzle flow and the CCD camera. It should also be noted that in this test, unlike the inlet measurements, the laser beam passes twice through the nozzle shear layer, which is likely to be the most turbulent portion of the nozzle flow.

Figure 32 shows plots of both the horizontal and vertical displacements of the laser spot during the test time of the TUSQ facility. Data is included from before the tunnel run to give an idea of the effect

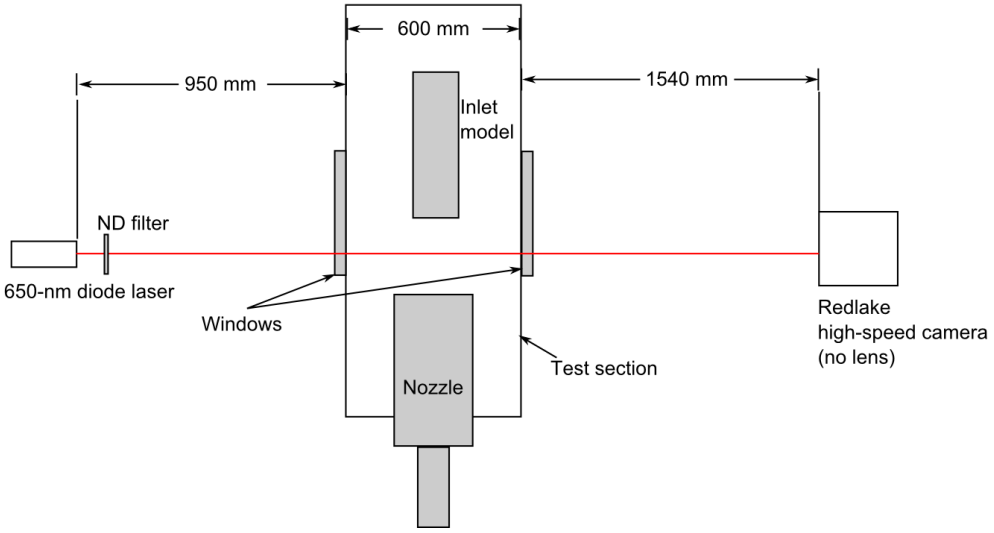

Figure 31: Beam steering measurement arrangement

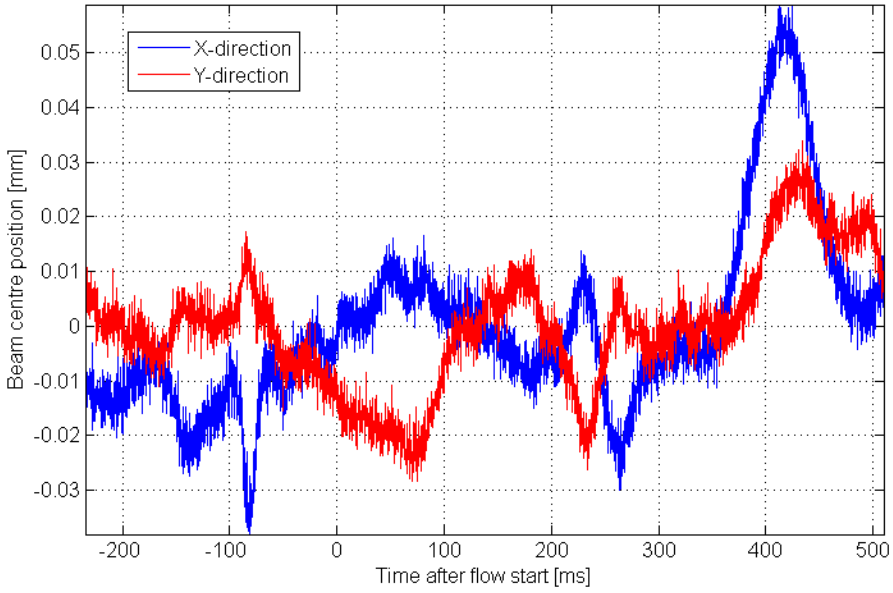

Figure 32: Displacement of laser spot position during tunnel run

of vibration on the spot location. The data clearly shows that the variations in the center of the laser beam are less than ± 0.02 mm during the test time, and are of similar amplitude to the variations before the test time, due mostly to vibrations in the laboratory. There is a larger variation in the y-position at the end of the tunnel run time, around 420 ms after the flow is initiated. This is most likely due to the flow termination processes in the tunnel. Even this displacement is less than 0.05 mm, which would be insufficient to change the signal on the photodetectors in the model. This indicates that beam steering due to turbulence was not a problem for these tests. The low density of the flow field ensures that any turbulent variations in the flow, though possibly significant in comparison to the flow density, will not be large enough to provide a noticeable displacement for the diode laser sensor that these conditions.

In addition to the experimental tests mentioned above, a calculation was performed to determine the effects of density changes due to shock waves. The conditions in the flat plate inlet were chosen because the post-shock conditions are constant and simpler to calculate than for the conical inlet case. Also, the density changes will be greater for the flat-plate configuration, and therefore the beam displacement at given conditions should also be larger.

The calculation considers flight at an altitude of 10 000 m. This would be a minimum altitude for scramjet flight, where the density gradients are likely to be at their largest. The tunnel conditions were not simulated for these calculations, because of a lack of data for temperatures below 233 K for the refractive index of air. Refractive index data as a function of temperature and pressure were obtained using the correlations of Ciddor (1996).

The beam path was traced through four passes through the inlet. Calculations of the beam positions were made through ray tracing through the optical system in the absence of density variations, accounting only for the reflections from the retroreflectors and refraction due to the inlet windows. This calculation provided a zero-displacement baseline against which the displacement due to density variations could be compared.

Post-shock conditions were calculated assuming $T_\infty = 223\,\mathrm{K}$ and $p_\infty = 26541\,\mathrm{Pa}$, the conditions at 10 000 m altitude according to the 1976 US standard atmosphere(Sissenwine et al. 1976), and assuming flight at Mach 5.8. For a 10 ° wedge, the shock angle will be 8 °. Using the oblique shock relations, the post-shock temperature and pressure at these conditions are $T_2 = 350.7\,\mathrm{K}$ and $p_2 = 102020\,\mathrm{Pa}$. Using the correlations of Ciddor (1996), the refractive indices of the air immediately before and after the oblique shock are $n_\infty = 1.000089028$ and $n_2 = 1.00022766$ respectively. The laser propagation direction is 55° to the freestream, as for the flat plate configuration tested in this report.

The deflection of the beam through the two shock waves can be determined using Snell's law, and it is this difference in refractive index, accumulated by passing eight times through the two shock waves that causes the displacement of the beam on the detector. If we ignore the density changes across the shock wave, the beam would have angles of 17° to the normal of the lower shock wave and 53° to the normal of the upper shock wave. Adapting the refractive indices, these angles change to 17.0024° and 52.9895° respectively for the first two shock waves. Propagating these angular displacements through all four passes through the inlet generates a displacement of less than 0.002 mm. This is negligible compared with the spatial dimensions of the detector.

Taken together, the experiment and calculation indicate that changes in refractive index due to either turbulent fluctuations or systematic deflection by shock waves do not cause beam displacements that are large enough to generate the fluctuations in signal that are evident in the absorption spectra obtained in the TUSQ facility. We now investigate the effects of vibration on the stability of the absorption signal over a scan.

8.2 Vibration Testing

As stated in Sec. 4.1, the absorption signal for the conical inlet condition should be approximately 2.3 times larger than that measured at the flat-plate condition. When the experiments were performed, however, the signal-to-noise ratio was lower than that for the flat-plate inlet tests. Section 8.1 indicates that the problem is unlikely to be caused by beam steering. It is more likely due to problems with the mounting of the laser/collimator arrangement, shown in Fig. 33.

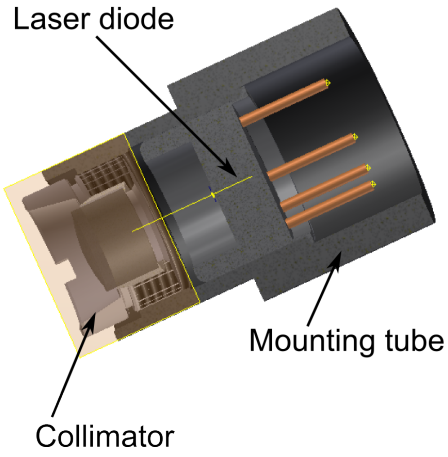

Figure 33: Laser/collimator assembly for conical inlet tests

The collimator is designed to be screw-mounted into a threaded tube, with the laser and socket held in place with a small set screw. The thread on the collimator was very fine, and the tube thread was too loose a fit. In order to hold the collimator in place, loctite adhesive was applied to the screw. It was noticed that during the evacuation of the tunnel the baseline signal level would begin to drift. This behavior may indicate that an air bubble may have expanded while the tunnel was being evacuated, changing the relative positions of the collimator and the laser very slightly. After passing through the inlet four times, even a slight change in this relative position would be sufficient to move the light beam to the edge of the detector, where the signal would be highly susceptible to vibration.

A procedure was developed that allowed the optics box to be tested, and is shown in Fig. 34. The arrangement consists of a Brüel and Kjær Type 4809 vibrating exciter, with a transducer attached to the side of the optics box, as close as possible to the location of the laser and collimator. The exciter provides a 45 N force with an amplitude of 8 mm at frequencies that could be varied by changing the AC input voltage signal, provided by a signal generator. In addition to the vibrating exciter, a pendulum of 0.25 m length and with a mass of 44.4 g at the end was used to provide an impulsive impact with an energy of 0.11 J to the inlet by holding the mass horizontally with the wire taut and then releasing it.

The effectiveness of the impulsive load test can be seen in Fig. 35. In this test one of the screws in the inlet system was loose, allowing motion of the laser/collimator system. The mass struck the inlet while absorption data was obtained at a ramp rate of 100 Hz. The plots are averaged baseline standard deviations during each of the scans after the initial impulsive excitation. The blue curve in Fig. 35 shows how the standard deviation of the background absorption signal rises sharply after the

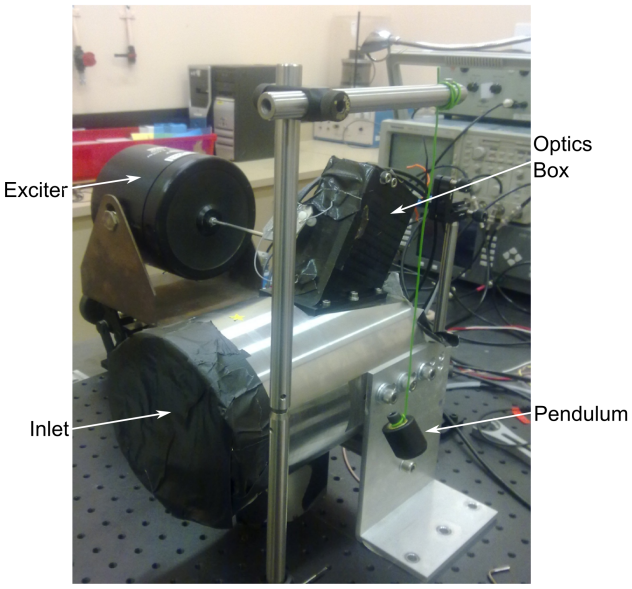

Figure 34: Vibration and impulse test apparatus

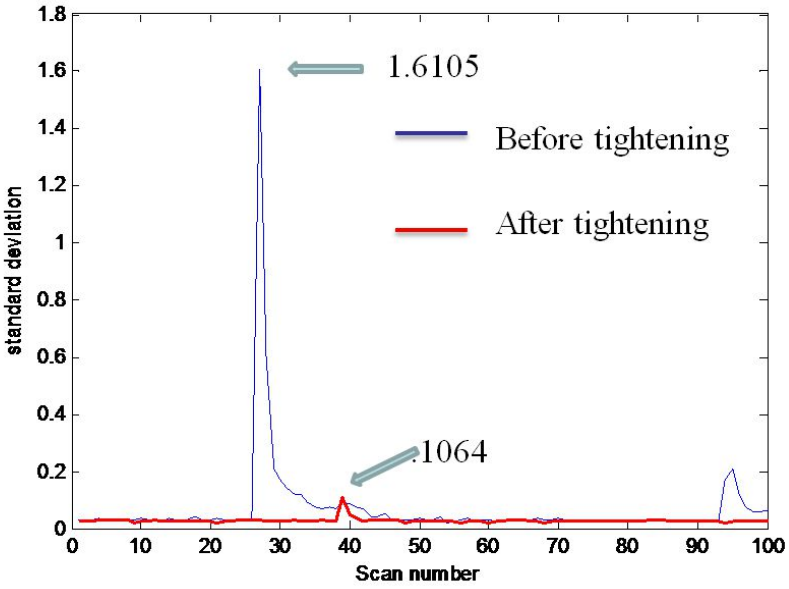

Figure 35: Impulse response plots

impulsive excitation during scan 26, decaying over the next 20 scans, or 0.2 seconds. The second peak near scan 93 is due to the pendulum mass bouncing off the side of the inlet and hitting the inlet a second time.

After tightening the set screw, the standard deviation upon impact is shown by the red line in Fig. 35. Tightening the screw caused a reduction in the standard deviation of the log-ratio output signal to a level that is 15 times smaller than the original deviation.

9 Conclusions

This report and its predecessor (O'Byrne 2010) describe the successful design, implementation and testing of two diode-laser-based sensors for the inlet of a supersonic combustion ramjet engine. The sensors were developed to be as simple as possible, using a single, widely tunable VCSEL and a folded anti-parallel path that could be fit into the confined spaces available in scramjet flight test payloads. The tunability of the VCSEL was intended to be used to determine the Mach number and angle of attack of the sensor based upon the different responses of the transitions within the tuning range of the laser. An analytical study of this behavior for a dual-wedge inlet showed that it was possible in principle to measure both of these quantities, although the system is much more sensitive to the freestream speed than to the angle of attack at the flight conditions.

Two inlet configurations were tested in a Mach 5.8 uniform flow in the TUSQ Ludwieg tube facility: an inlet composed of a pair of flat plates angled at 10° to the flow, and a conical inlet with a compression angle of 7.2°, based upon the model expected to fly as part of the SCRAMSPACE program in 2012. In both cases, very precise freestream velocity measurements were obtained at a rate of 150 measurements per second, limited mostly by the bandwidth of the log-ratio detector. The measurement rate for the flat-plate configuration was closer to 400 per second because four transitions were measured in each scan, and a velocity measurement can be made for each of these four transitions. Between single scans, the velocity standard deviation for the flat-plate was 40 m/s or roughly 4% for the flat-plate inlet measurements. Averaged over the test time, the run-to-run variability in the velocity was $\pm 0.8\%$ and for the temperature was ± 40 K. The larger uncertainty in the temperature is due to the significant noise superimposed upon the signal.

Although the conical inlet optical system was designed to give better vibration isolation and higher signals than the flat-plate measurement, the signals measured by the conical inlet model had even more noise than the flat-plate inlet results. In addition to the greater noise, the amplifier began to oscillate during the tests, allowing the absorbance from only two transitions to be recorded. Despite the signal-to-noise ratio being only 2:1, compared to the 5:1 measured for the flat-plate inlet, the uncertainty in velocity was also around ± 40 m/s, because the uncertainty in velocity depends only weakly on the addition of Gaussian amplitude noise to the signal. Because at most only two transitions were recorded for any of the tunnel runs, we were unable to measure freestream temperature for the conical inlet tests.

The most likely two reasons for the poorer performance of the conical inlet were possible beam steering due to the shock layers or turbulent freestream fluctuations or the effect of vibration on the optical system. Beam steering was tested for experimentally and predicted based upon the calculated flowfields and was found to be negligible for both cases. The most likely reason for the variation in signal during the tunnel runs was the mounting between the laser and collimator in the conical system, as this is the most sensitive part of the system design to small displacements in the optics. The fine thread of the collimator did not perfectly match the mounting tube, and adhesive was used to keep it in place. Variations in signal during the evacuation of the facility before a run suggest that small bubbles in the adhesive may have expanded, causing a small displacement of the beam on the signal photodiode and making the system susceptible to vibration noise. A vibration and impact testing

arrangement has since been implemented to allow vibration problems to be examined in a controlled manner.

Initial tests with the conical inlet did not show the splitting of the Doppler-shifted peaks that should be expected for a hypersonic inlet. This was because the compression ratio was too great, and there was a small step in the downstream portion of the inlet. These influences caused the flow to choke and behave as a highly turbulent subsonic flow. The model was cut at the downstream end, reducing the area contraction of the inlet, and this change generated the expected Doppler-shifted peaks characteristic of hypersonic inlet flow. Schlieren images corroborated these results, showing a normal shock in front of the inlet for the cases where the diode laser sensor indicated choked inlet flow.

A wavelength modulation system was implemented and absorption was measured in ambient air, using the conical inlet optical path and hardware. Both 1f and 2f wavelength-modulated signals were obtained over four transitions, with the ramp removed from the detected signal. The signal-to-noise ratio of these preliminary measurements, while better than that of direct absorption, was not as good as that of the log-ratio detector and in its current unoptimized form insufficient to get a single-scan measurement at hypersonic high-altitude flight conditions. The system was comfortably able to scan at kHz rates, which is significantly faster than the log102-based detector. While the log ratio detector was the more precise of the two detectors, and provides a direct measurement of absorbance that can be used to determine temperatures, the speed of the wavelength modulation detector and the lack of a reference beam are advantages of this system. We also successfully built a prototype wavelength modulation detection system and tested that system with calibrated current inputs.

Acknowledgments

This work was funded by the US Air Force Asian Office of Aerospace Research and Development (AOARD) grant 084019 and the authors gratefully acknowledge this. We thank Associate Professor David Buttsworth for running the tests in the University of Southern Queensland's Ludwieg tube facility. We also acknowledge the excellent fabrication assistance we received from the School of Engineering and Technology's technical and workshop staff.

References

Allen, M. G. (1998), 'Diode laser absorption sensors for gasdynamic and combustion flows', *Measurement Science and Technology* **9**, 545–562.

Allen, M. G., Parker, T. E., Reinecke, W. G., Legner, H. H., Foutter, R. R., Rawlins, W. T. and Davis, S. J. (1993), 'Fluorescence imaging of OH and NO in a model supersonic combustor', *AIAA Journal* **31**(3), 505–512.

Anderson, J. D. (1990), *Modern Compressible flow with Historical Perspective*, 2^{nd} edn, M^{c}Graw-Hill.

Barhorst, T., Williams, S., Chen, S., Page, M. E., Silver, J. A., Sappey, A., McCormack, P., Masterson, P., Zhao, Q., Sutherland, L., Smith, I., van Houdt, P., Hannam, J. and Owenby, D. (2009), Development of an in-flight, non-intrusive mass capture system, *in* 'AIAA Paper 2009-5067'. 45^{th} AIAA/ASME/SAE/ASEE Joint Propulsion Conference and Exhibit, 2–5 August, Denver Colorado.

Boyce, R. R., Gerard, S. and Paull, A. (2003), The HyShot scramjet flight experiment - flight data and CFD calculations compared, *in* 'AIAA Paper 2003-7029'. 12^{th} AIAA International Space Planes and Hypersonic Systems and Technologies Conference, Norfolk, VA.

Brown, M. S. and Barhorst, T. F. (2011), Post-flight analysis of the diode-laser-based mass capture experiment onboard HIFiRE flight 1, *in* 'AIAA 2011-2359', 17^{th} AIAA International Space Planes and Hypersonic Systems and Technologies Conference, 11–14 April, 2001, San Francisco, California.

Buttsworth, D. R., Balage, S. and Widodo, A. (2011), HIFiRE 3 scramjet inlet testing in TUSQ facility: Mach 6 nozzle exit pitot survey. Personal communication.

Buttsworth, D. R. and Smart, M. K. (2010), Development of a Ludwieg tube with free piston compression heating for scramjet inlet starting experiments, *in* 'AIAA 2010-0588', Orlando, FL. 48^{th} Aerospace Sciences Meeting Including the New Horizons Forum and Aerospace Exposition.

Buttsworth, D. R. and Widodo, A. (2010), Stagnation temperature measurements in a hypersonic wind tunnel using the sodium line-reversal method, *in* 'Proceedings of the 17^{th} Australasian Fluid Mechanics Conference, 5–9 December, Auckland, New Zealand'.

Chang, L. S., Jeffries, J. B. and Hanson, R. K. (2010), 'Mass Flux Sensing via Tunable Diode Laser Absorption of Water Vapor', *AIAA Journal* **48**, 2687–2693.

Ciddor, P. E. (1996), 'Refractive index of air: New equations for the visible and near infrared', *Applied Optics* **35**, 1566–1573.

Curran, E. T., Heiser, W. H. and Pratt, D. T. (1996), 'Fluid phenomena in scramjet combustion systems', *Annual Review of Fluid Mechanics* **28**(1), 323–360.
URL: *http://www.annualreviews.org/doi/abs/10.1146/annurev.fl.28.010196.001543*

Cutler, A. D., Danehy, P. M., Springer, R. R., O'Byrne, S., Capriotti, D. P. and DeLoach, R. (2003), 'Coherent anti-Stokes Raman spectroscopic thermometry in a supersonic combustor', *AIAA Journal* **24**(4), 487–507.

Eckbreth, A. C., Anderson, T. J. and Dobbs, G. M. (1988), 'Multi-color CARS for hydrogen-fueled scramjet applications', *Applied Physics B: Lasers and Optics* **45**, 215–223. 10.1007/BF00687149.
URL: *http://dx.doi.org/10.1007/BF00687149*

Ferri, A. (1964), 'Review of the problems in application of supersonic combustion', *Journal of the Aeronautical Society* **64**, 575–597.

Furlong, E. R., Baer, D. S. and Hanson, R. K. (1998), 'Real-time adaptive combustion control using diode-laser absorption sensors', *27th Symposium (International) on Combustion* **27**(1), 103 – 111. Twenty-Seventh Sysposium (International) on Combustion Volume One.
URL: *http://www.sciencedirect.com/science/article/pii/S0082078498803950*

Griffiths, A. D. and Houwing, A. F. P. (2005), 'Diode laser absorption spectroscopy of water vapor in a scramjet combustor', *Applied Optics* **44**(31), 6653–6659.

Gruber, M. R., Dunbar, J. M., Carter, C. D. and Hsu, K. Y. (2004), 'Mixing and combustion studies using cavity-based flameholders in a supersonic flow', *Journal of Propulsion and Power* **20**(5), 769–778.

He, Y. and Morgan, R. G. (1994), 'Transition of compressible high-enthalpy boundary layer flow over a flat plate', *The Aeronautical Journal* **98**(2), 25–33.

Kantrowitz, A. N. and Donaldson, C. N. (1945), Preliminary investigation of supersonic diffusers, Technical report, NACA ACR L5D20.

Lyle, K. H., Jeffries, J. B., Hanson, R. K. and Winter, M. (2007), 'Diode-laser sensor for air-mass flux 2: Nonuniform flow modeling and aeroengine tests', *AIAA Journal* **45**, 2213–2223.

McClinton, C. (2006), X-43 — scramjet power breaks the hypersonic barrier, *in* 'AIAA Paper 2006-1'. 44th AIAA Aerospace Sciences Meeting and Exhibit, 9–12 January, 2006, Reno NV.

McIntyre, T. J., Houwing, A. F. P., Palma, P. C., Rabbath, P. A. B. and Fox, J. S. (1997), 'Optical and pressure measurements in shock tunnel testing of a model scramjet combustor', *Journal of Propulsion and Power* **13**(3), 388–394.

McMillin, B. K. (1993), Instantaneous two-line PLIF temperature imaging of nitric oxide in supersonic mixing and combustion flowfields, PhD thesis, Stanford University.

Miller, M. F., Kessler, W. J. and Allen, M. G. (1996), 'Diode laser-based air mass flux sensor for subsonic aeropropulsion inlets', *Appl. Opt.* **35**(24), 4905–4912.
URL: *http://ao.osa.org/abstract.cfm?URI=ao-35-24-4905*

O'Byrne, S. B. (2010), Diode laser sensor for scramjet inlets, Technical report, US Air Force Asian Office of Aerospace Research and Development Report AOARD-08-4019.

O'Byrne, S. B., Danehy, P. M., Cutler, A. and Tedder, S. (2007), 'Dual-pump CARS temperature and species concentration measurements in a supersonic combustor', *AIAA Journal* .

O'Byrne, S., Stotz, I., Neely, A. J., Boyce, R. R. and Houwing, A. F. P. (2005), 'OH PLIF imaging of supersonic combustion using cavity injection', *AIAA Paper 2005-3357* . Proceedings of the AIAA/CIRA 13th International Space Planes and Hypersonics Systems and Technologies Conference, Capua, Italy, May 16–20, 2005.

O'Byrne, S. and Wittig, S. M. (2008), Measurement of hypersonic inlet flow using tuneable diode laser absorption spectroscopy, *in* 'Proceedings of the 8th Australian Space Science Conference'.

Quine, B. M. and Drummond, J. R. (2002), 'GENSPECT: a line-by-line code with selectable interpolation error tolerance', *Journal of Quantitative Spectroscopy and Radiative Transfer* .

Rothman, L. S., Jacquemart, D., Barbe, A., Benner, D., Birk, M., Brown, L. R. and Carleer, M. R. (2005), 'The HITRAN 2004 molecular spectroscopic database', *Journal of Quantitative Spectroscopy and Radiative Transfer* **96**(2), 139–204.

Sanders, S., Wang, J., Jeffries, J. B. and Hanson, R. K. (2001), 'Diode laser absorption sensor for line-of-sight temperature distributions', *Applied Optics* **40**(24), 4404–4415.

Silver, J. A. (1992), 'Frequency-modulation spectroscopy for trace species detection: theory and comparison among experimental methods', *Appl. Opt.* **31**(6), 707–717.
URL: *http://ao.osa.org/abstract.cfm?URI=ao-31-6-707*

Sissenwine, N., Dubin, M. and Teweles, S. (1976), U.S. standard atmosphere, 1976, Technical Report Stock Number 003-017-00323-0, US Government Printing Office, Washington DC, USA.

Smart, M. (2001), 'Experimental testing of a hypersonic inlet with rectangular-to-elliptical shape transition', *Journal of Propulsion and Power* **17**(2), 276–283.

Tahir, R., Molder, S. and Timofeev, E. (2003), Unsteady starting of high Mach number air inlets — a CFD study, *in* 'AIAA Paper 2003-5191'. 39^{th} AIAA/ASME/SAE/ASEE Joint Propulsion Conference and Exhibit Powered Flight The Next Century, Huntsvill, Al.

Upschulte, B. L., Miller, M. F. and Allen, M. G. (2000), 'Diode laser sensor for gasdynamic measurements in a model scramjet combustor', *AIAA Journal* **38**(7), 1246–1252.

van Wie, D. M. (2000), *Scramjet Inlets*, Vol. 189 of *Progress in Aeronautics and Astronautics*, AIAA, chapter 7, pp. 447–511.

Vereschagin, K. A., Smirnov, V. V., Stelmakh, O. M., Fabelinsky, V. I., Sabelnikov, V. A., Ivanov, V. V., Clauss, W. and Oschwald, M. (2001), 'Temperature measurements by coherent anti-Stokes Raman spectroscopy in hydrogen-fuelled scramjet combustor', *Aerospace Science and Technology* **5**(5), 347 – 355.
URL: *http://www.sciencedirect.com/science/article/pii/S1270963801011087*

Weber, R. J. and MacKay, J. S. (1958), 'An analysis of ramjet engines using supersonic combustion'.

Webster, L., O'Byrne, S. and Houwing, A. F. P. (2005), Determination of temperature distributions in air using a scanning vertical-cavity surface-emitting laser, *in* 'Proceedings of the 4^{th} Austraian Conference on Laser Diagnostics in Fluids Mechanics and Combustion'.

Williams, S., Barone, D., Barhorst, T., Jackson, K. and Lin, K.-C. (2006), Diode laser diagnostics of high speed flows, *in* 'AIAA 2006-7999', Canberra, Australia. AIAA International Space Places and Hypersonic Systems and Technologies Conference.

Wittig, S. M. and O'Byrne, S. (2011), Characterisation of supersonic combuster inlet flows using diode laser absorption spectroscopy, *in* 'AIAA paper 2011-0073'. 48^{th} AIAA Aerospace Sciences Meeting, Orlando, FL, 4–7 January,.

Zander, R. (1973), 'Water vapor above 25 km altitude', *Pure and Applied Geophysics* **106–108**, 1346–1351.
URL: *http://dx.doi.org/10.1007/BF00881089*

Zhao, X., Jiu, X., Jeffries, J. B. and Hanson, R. K. (2003), 'Development of a sensor for temperature and water concentration in combustion gases using a single tuneable diode laser', *Measurement Science and Technology* **14**, 1459–1468.

Appendix

The following sections outline the personnel supported, and the measurable outcomes of this project and the previous AOARD project related to it over the period 2008–2010.

A. Personnel Supported

The main investigators on this project were Chief Investigator Dr. S. O'Byrne, Ph.D. candidate S. M. Wittig, PhD candidate Y. Krishna, Research Associate Dr. J. Kurtz and Electronics Engineer Dr. M. Aizengendler. Additional support and advice was received from Prof. R. Boyce and Dr. T. McIntyre from the University of Queensland.

The University of Southern Queensland's Ludwieg tube facility, operated by Assoc. Prof. David Buttsworth, was supported by this grant, providing the hypersonic conditions in which the sensor could be tested.

B. Publications

- S. O'Byrne, S. M. Wittig, "Measurement of hypersonic inlet flow using diode laser absorption spectroscopy," Proceedings of the 8^{th} Australian Space Sciences Conference, September 29–October 1, 2008, Canberra, Australia.

- J.P. Long, S. O'Byrne and A.J. Neely , "Two-dimensional heat transfer analysis of a generic Scramjet inlet," Proceedings of the 8^{th} Australian Space Sciences Conference, September 29–October 1, 2008, Canberra, Australia.

- A. Hohmann, S. O'Byrne, "Oxygen linestrength measurements in a high-temperature gas cell," Proceedings of the 5^{th} Australian Conference on Laser Diagnostics in Fluid Mechanics and Combustion, December 1–3, 2008, Perth, Australia.

- L. Huynh and S. O'Byrne, "Water Vapour Absorption Spectroscopy in a Simulated Helicopter Exhaust using Vertical-Cavity Surface-Emitting Lasers" AIAA Student Conference, Melbourne, Australia, October 2009.

- S. O'Byrne, L. Huynh, S. M. Wittig and N. S. A. Smith, "Non-intrusive Water Vapour Absorption Measurements in a Simulated Helicopter Exhaust", Proceedings of the Australian Combustion Symposium, Brisbane, Australia, December 2–4, 2009.

- L. Huynh and S. O'Byrne, "Water Vapour Absorption Spectroscopy in a Simulated Helicopter Exhaust using Vertical-Cavity Surface-Emitting Lasers" AIAA paper 2010-1599, 48^{th} AIAA Aerospace Sciences Meeting Including the New Horizons Forum and Aerospace Exposition, Orlando, Florida, Jan. 4–7, 2010 (Same content as above paper, re-presented by invitation).

- S. Wittig and S. O'Byrne, "Characterization of Supersonic Combustor Inlet Flows Using Diode Laser Absorption Spectroscopy" AIAA paper 2011-0073, 49^{th} AIAA Aerospace Sciences Meeting Including the New Horizons Forum and Aerospace Exposition, Orlando, Florida, Jan. 4–7, 2011
- S. Wittig and S. O'Byrne, " Diode Laser Absorption Measurement of Oxygen Velocity and Temperature in a Simulated Hypersonic Inlet Flow" In preparation.

C. Interactions

This work was presented at the following meetings:

- The 8^{th} Australian Space Science Conference, Canberra, December 2008.
- The 5^{th} Australian Combustion Symposium, Brisbane, December 2009.
- The AIAA Student Conference, October 2009.
- The 5^{th} Australian Conference on Laser Diagnostics in Fluid Mechanics and Combustion, Perth, December 2008.
- The 48^{th} AIAA Aerospace Sciences Meeting, Orlando, Florida, January 2010.
- The 49^{th} AIAA Aerospace Sciences Meeting, Orlando, Florida, January 2011.
- The 11^{th} International Workshop on Shock Tube Technology, Brisbane, Australia, March 2011.
- Invited talks at NASA Langley Research Center, the Air Force Research Laboratories and Purdue University.

D. Inventions

No patent applications have been made at present, but notification of IP for one aspect of the apparatus has been declared to NewSouth Innovations, the commercialization arm of UNSW.

E. Honors/Awards

The following honors and awards have been received by work related to this project over the three year period of AOARD funding:

- This AOARD support has in part led to a successful application to the Australian Space Research Program for AUD 5 Million in funding for a flight test, including AUD 794 000 for development of the diode laser absorption sensor, concentrating on testing a sensor like the one produced here on a hypersonic flight test in 2012.

- The paper 'Water Vapour Absorption Spectroscopy in a Simulated Helicopter Exhaust using Vertical-Cavity Surface-Emitting Lasers' by L. Huynh and S. O'Byrne won the best paper award at the Australasian Branch of the AIAA Student conference.
- PhD Student S. Wittig won a 2000 UK pound competitive stipend from the Royal Aeronautical Society to perform tests at subsonic and transonic speeds in the DSTO transonic facility using O_2 diode laser absorption spectroscopy.
- The presentation 'Taming the beast: the role of non-intrusive laser diagnostics in vehicle emissions measurement' by S. Wittig won a $1 000 prize for best presentation at the UNSW energy showcase in Sydney, Australia in 2010.

F. Lock-In Amplifier Design Details

1. Specifications

General

- Absorbance Measurement $<10^{-4}$
- Bandwidth 5MHz

Signal Input

- Single-ended current input Low impedance (50Ý photodiode load)
- Photodiode Bias Voltage Output $5.0V_{DC}$
- Voltage Gain 80dB
- Bandwidth 5 MHz
- Low noise <6.0nV/ãHz

Reference Input

- Voltage Gain 0 - 9.5dB
- Phase shift 0º - 360º (2 stages of 0º - 180º)
- Phase shifter resolution Continuous
- Bandwidth 5 MHz

Output

- Time constant ($1/f_{3dB}$) TBD
- Roll-off Up to 24dB/octave (80dB/decade)
- Voltage Gain 9.5dB (max)
- DC offset control ±1.5V
- Voltage Output ±3V

Phase Detector

2F Mode 2 x Reference frequency

Power Supply

±5V @ 200mA

2. PCB Schematics

The lock-in amplifier design comprises six sub-circuits including:

1. Input Stage
2. Bandpass Filter
3. Reference Input
4. Phase Detector
5. Output Filter/Amplifier
6. Power and Reference Voltages

These sub-circuits, as depicted in Figure 1 below, are described in the following sections.

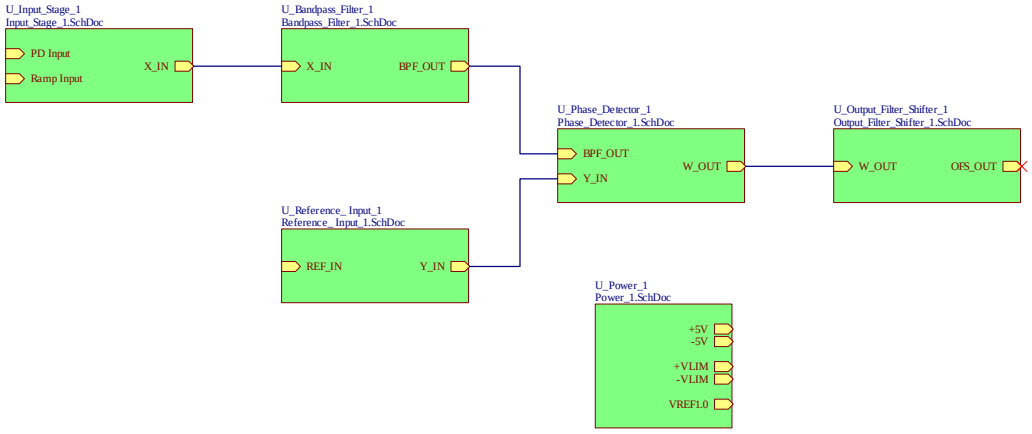

Figure 1. Lock-in Amplifier Block Diagram

2.1 Input Stage

The input stage comprises the following sub-circuits:

- Photodiode preamplifier;
- Ramp preamplifier;
- Amplifier/Ramp Subtracter.

The photodiode preamplifier provides a 50Ý load for the photodiode current and a conventional wide bandwidth, low-noise, low offset linear voltage amplifier (U1). The nominal maximum voltage gain of this stage is 30dB and can be adjusted by R2. The offset voltage can be adjusted by ±50mV via R4. The prototype circuit employs an AD8055, however, a better choice would be an OPA620 that has better noise and voltage offset characteristics.

The ramp amplifier (U3) is much the same as the photodiode amplifier, but does not require the same gain. Voltage gain and offset trimming is provided by R19 and R21, respectively. The ramp signal is intended to reflect the current ramp used the sweep the laser wavelength so that this can be removed from the photodiode signal prior to detection in the multiplier.

The second gain stage (U2) is a differential amplifier that provides an extra 30dB of gain to the photodiode signal and also subtracts the ramp component from the input signal.

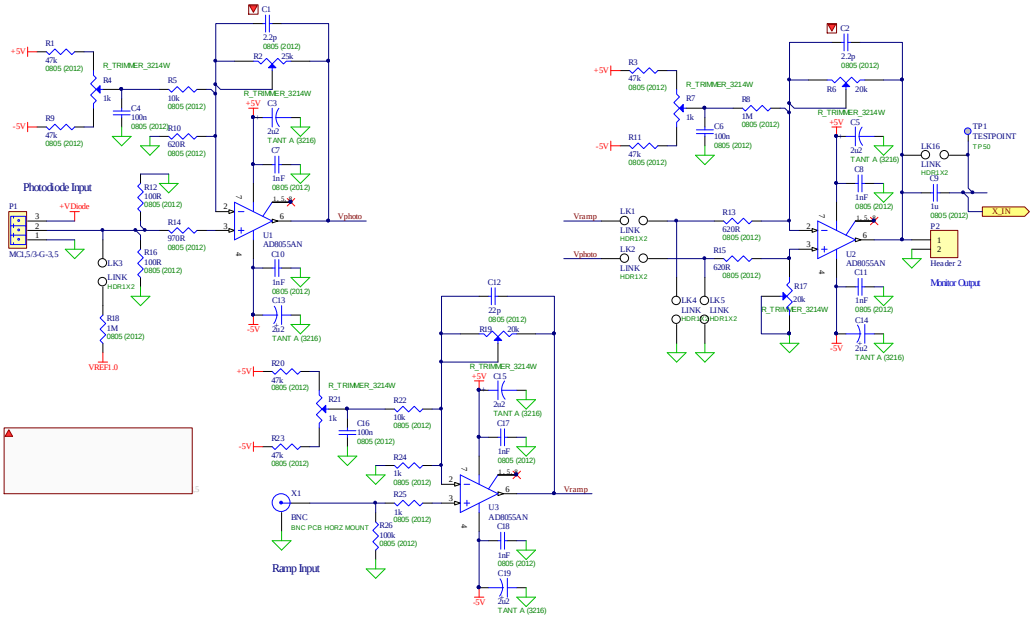

Figure 2. Input Stage

2.2 Bandpass Filter

The bandpass filter is employed to band-limit the undesirable noise components in the input signal prior to being mixed with the reference signal in the detector sub-circuit. It also provides extra gain to the input signal. It is based on a biquad bandpass design with independently variable gain, bandwidth and centre frequency provided by R79, R77 and R74/R75, respectively.

With the default component values, the following parameters are expected:

- Voltage gain is variable between -15dB and +20dB;
- Bandwidth variable between 50kHz and 500kHz;
- Centre frequency variable between 700kHz and 4MHz.

Links LNK14 and LNK15 are provided to bypass or include the filter in the signal path.

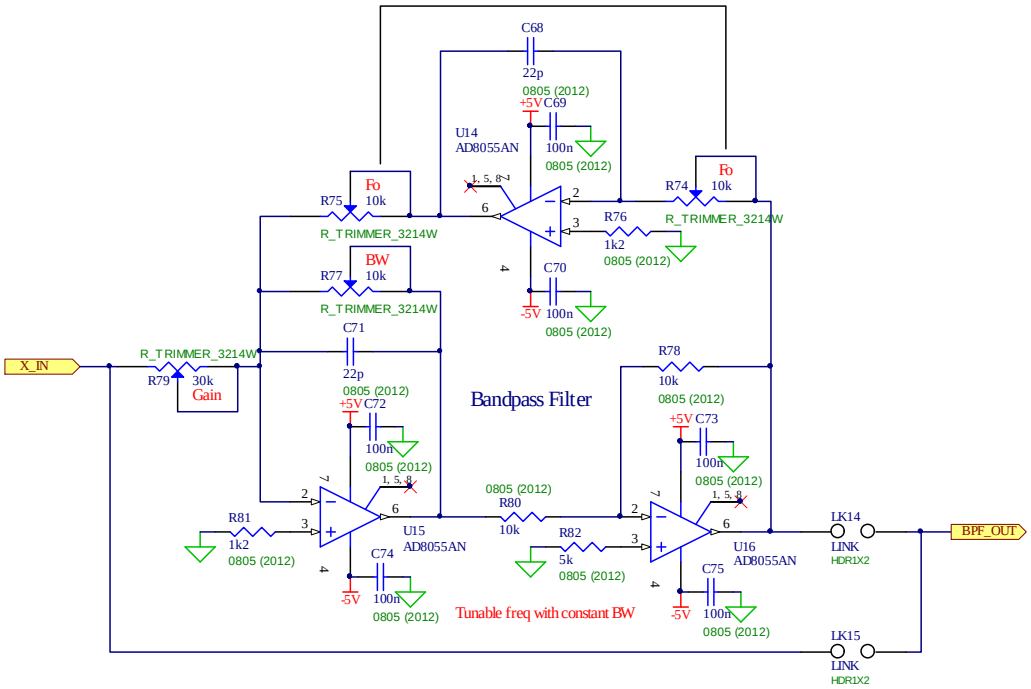

Figure 3. Band Pass Filter

2.3 Reference Input Amplifier & Phase Shifter

The reference input is derived from the same modulation signal that is superimposed on the laser current ramp. However, for 2F detection, the reference frequency must be twice the modulation frequency. This can be achieved by employing a dual channel function generator. For the lock-in amplifier to provide optimal detection, the 2F reference signal must be in phase with the 1F modulation signal.

The input buffer/amplifier (U6) provides a voltage gain of up to ~9dB. The following two stages (U5 and U4) are unity gain phase shifters that provide ~180º of phase shift each. The phase shift is controlled by R36 and R34.

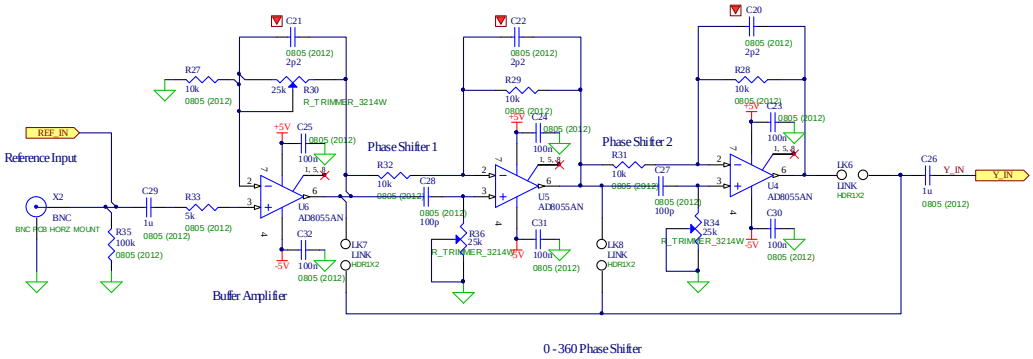

Figure 4. Reference Input Stage

2.4 Lock-in Detector Multiplier

The lock-in detector (U7) is based around an Analog Devices AD835 multiplier IC. A maximum voltage gain of ~12dB (x4) is available via R50 and R48. An output frequency response in excess of 20MHz is achievable.

The two input amplifiers (U8 and U9) have preset voltage gains of 6dB (x2), but have independent DC offset control via R38 and R45, respectively. It is important to note here that any DC level in the input or reference signals will adversely affect the multiplier output.

Adjustment of the DC offset on the signals at VX and VY to zero is critical for optimum detector operation. If there is any significant DC offset input to the multiplier, the resulting output will contain a significant component of the reference signal.

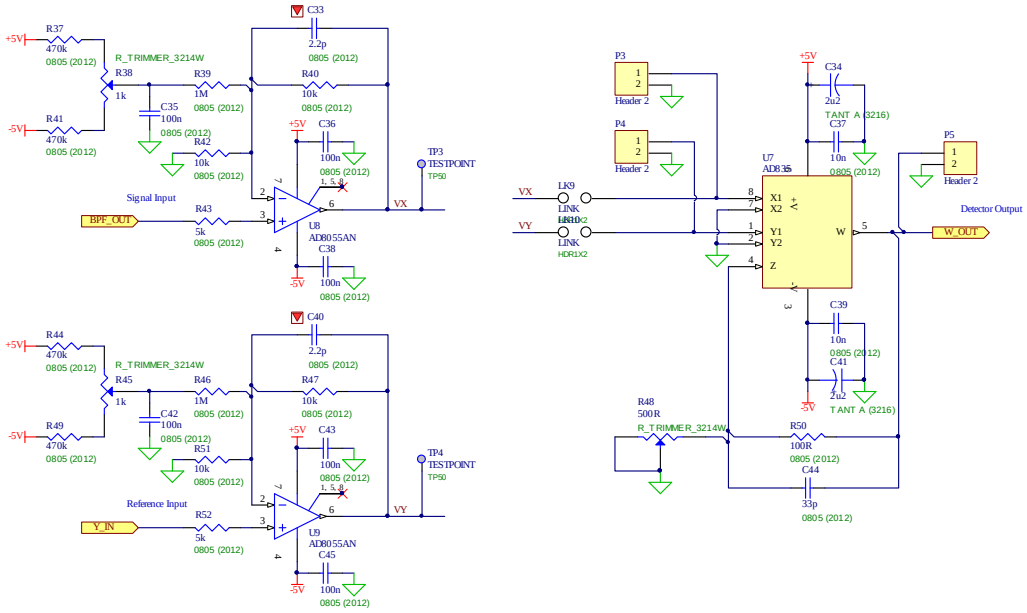

Figure 5. Lock-in Detector Multiplier

2.5 Output Lowpass Filter and Amplifier/Shifter

The output lowpass filter comprises two cascaded 2-pole stages formed by U11 and U10. The respective rolloff frequencies are determined by R56/C49 and R55/C52 in the first stage; R54/C48 and R53/C50 in the second stage. Links LK13, LK11 and LK12 facilitate the selection of filter stages in the signal chain.

The output amplifier (U12) has a maximum voltage gain of ~9.5dB (x3) controlled by R62. DC offset trimming is also available via R61.

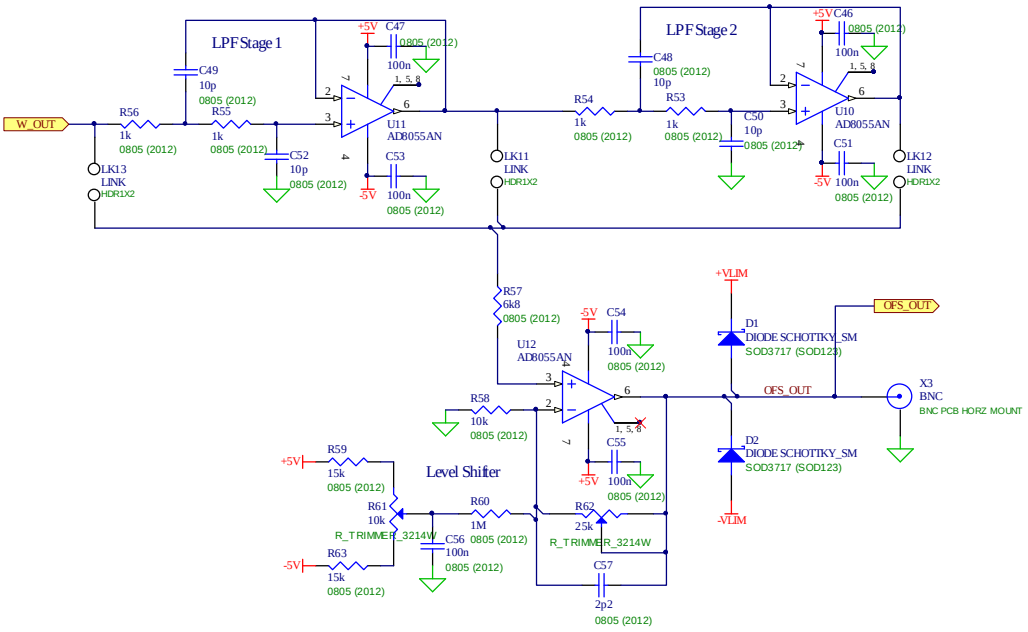

Figure 6. Output Filter/Amplifier Stage

2.6 Power & Reference Voltages

The power and reference voltage stage provides the following:

- receives the external ±5V supply voltage;
- provides the photodiodeôs +5V_{DC} bias voltage;
- generates a 1.0V_{DC} test reference voltage (Adjustable to suit application via R67);
- generates ±3V_{DC} output clamp voltages (Adjustable to suit application via R66 and R71).

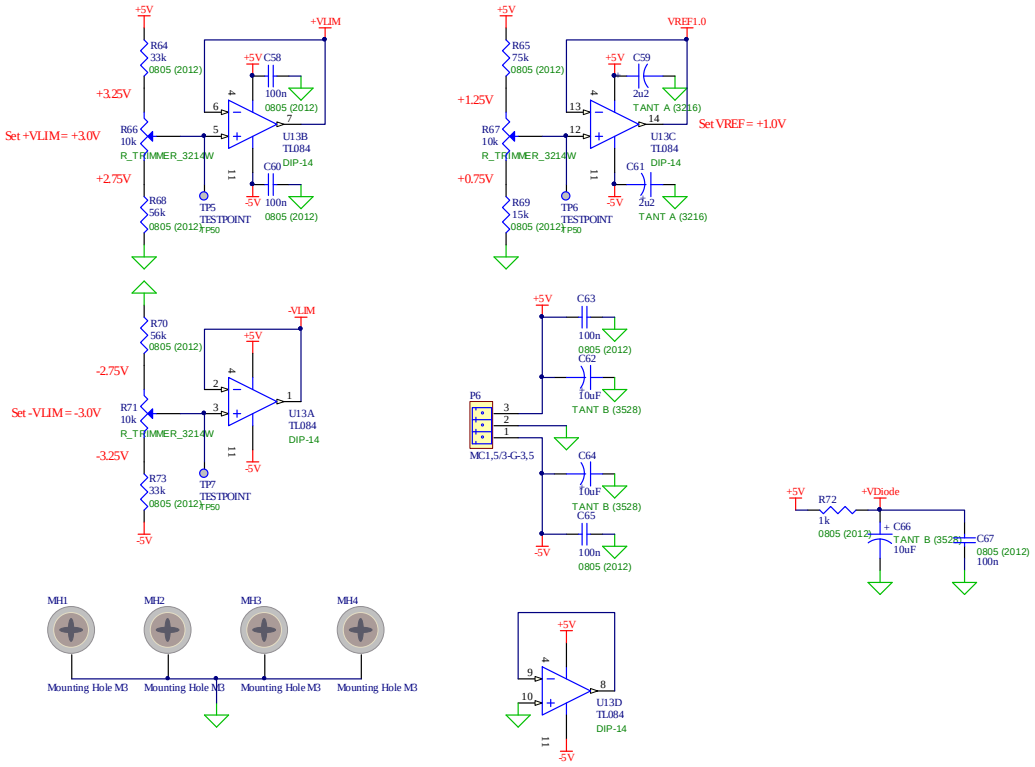

Figure 7. Power & Reference Voltage Stage

Place four A4/A3 Schematics here

3. PCB Layout

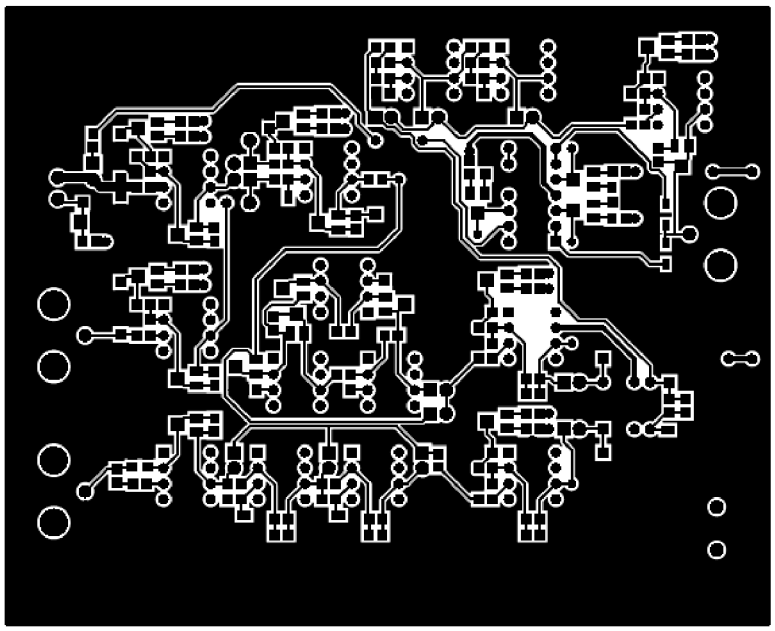

Figure 8. PCB Top Layer

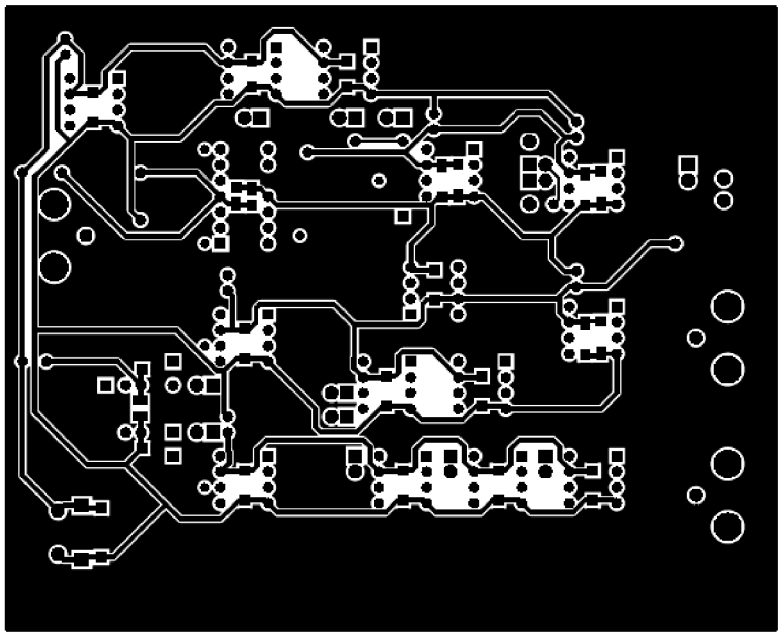

Figure 9. PCB Bottom Layer

4. Mechanical CAD

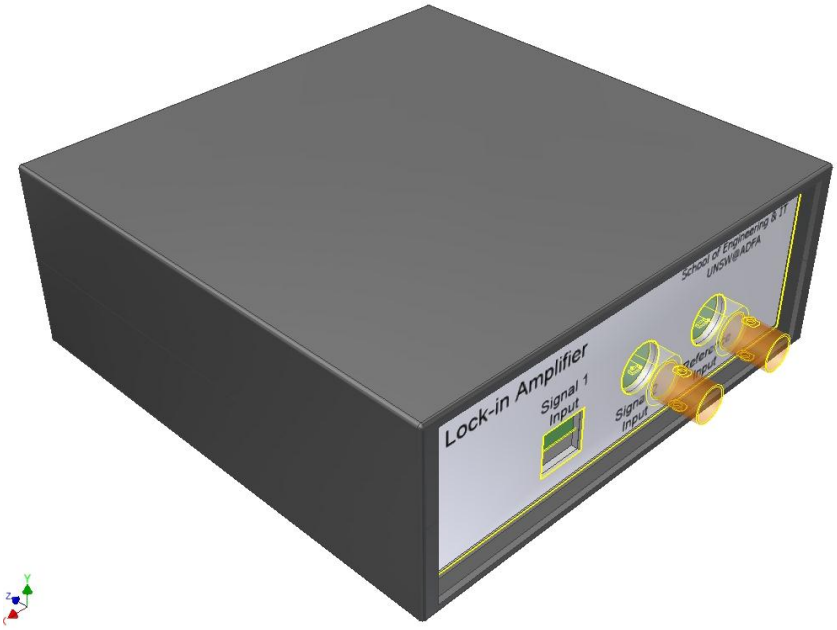

Figure 10a. Case front oblique view (closed)

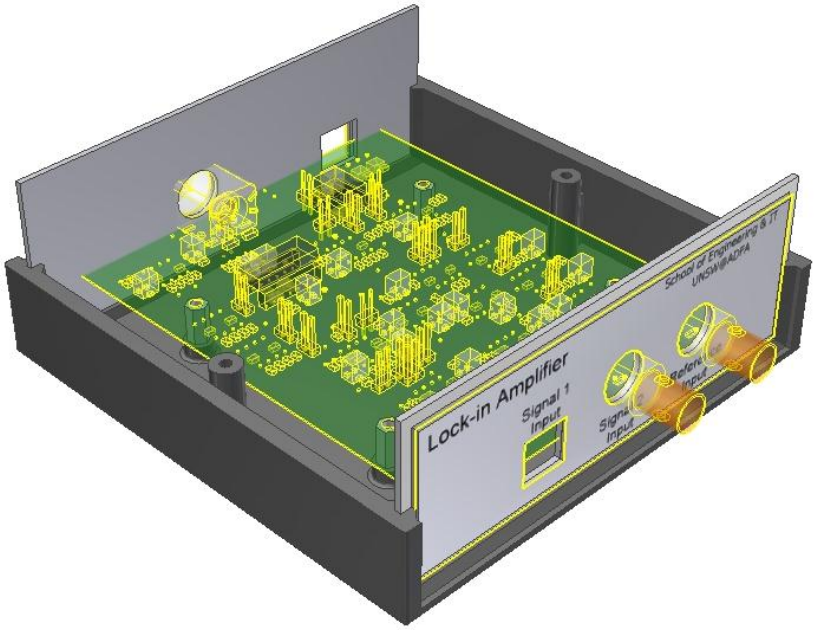

Figure 10b. Case front oblique view (open)

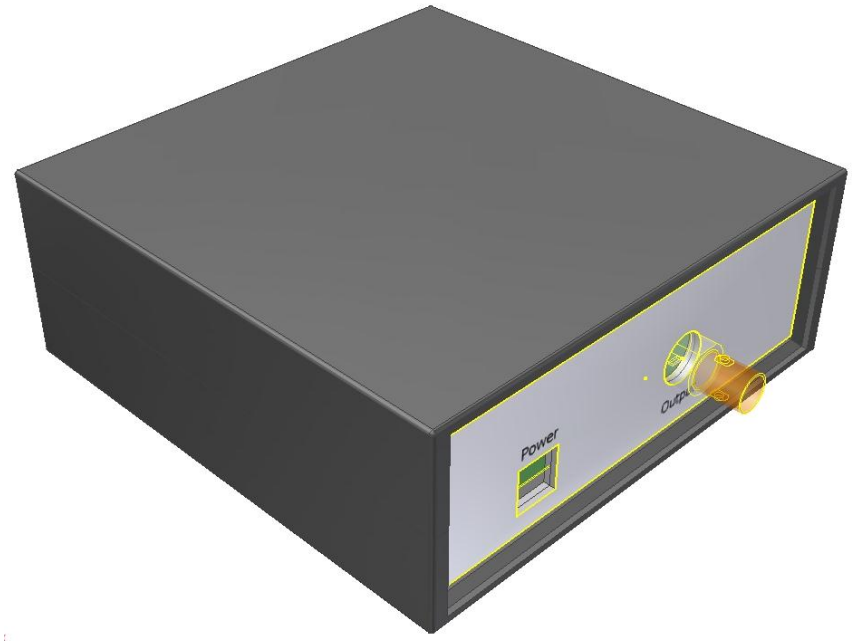

Figure 11a. Case rear oblique view

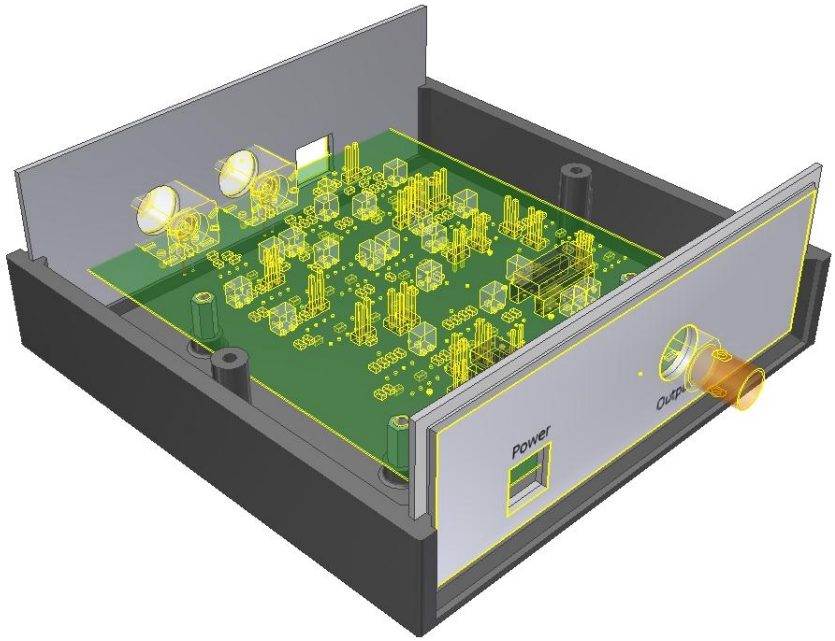

Figure 11a. Case rear oblique view

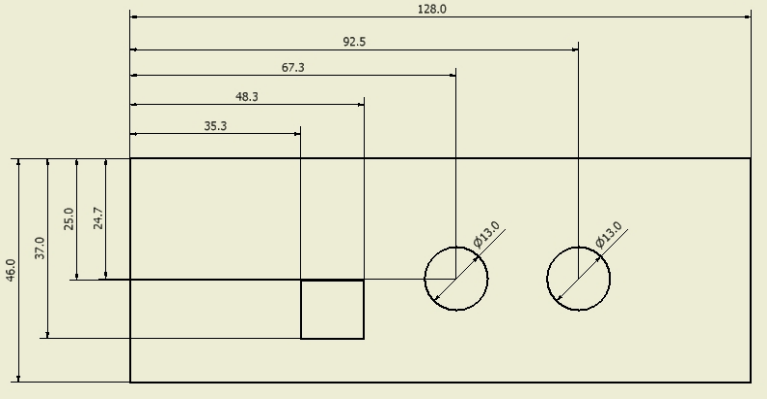

Figure 12a. Front Panel Drawing

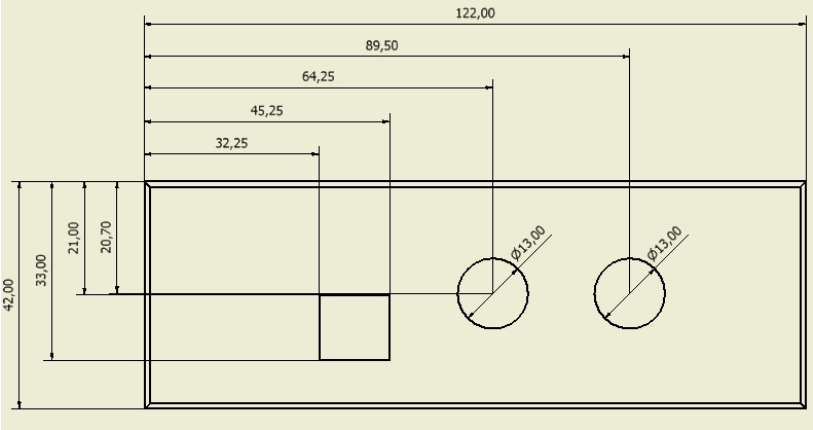

Figure 12b. Front Label Drawing

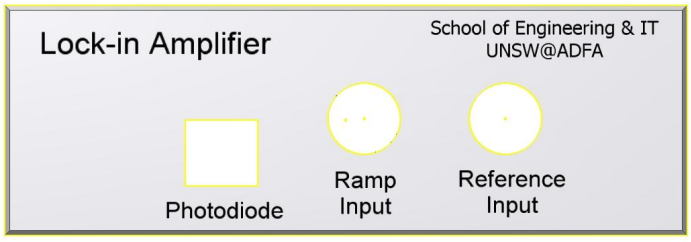

Figure 12c. Front Label

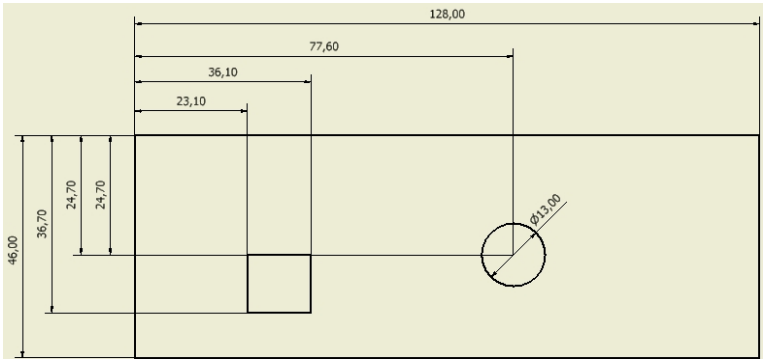

Figure 13a. Rear Panel Drawing

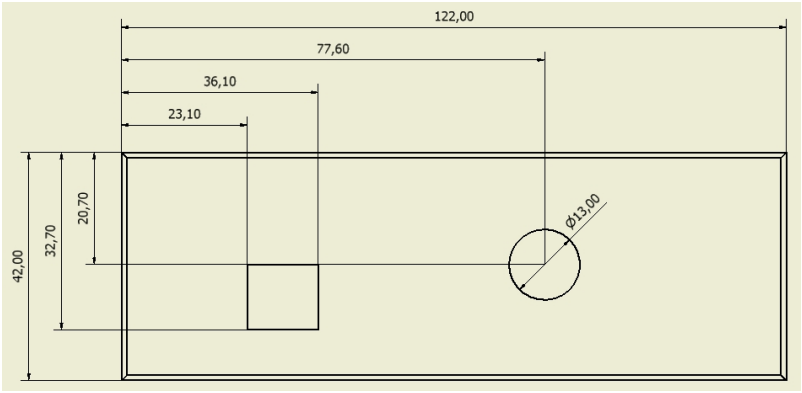

Figure 13b. Rear Label Drawing

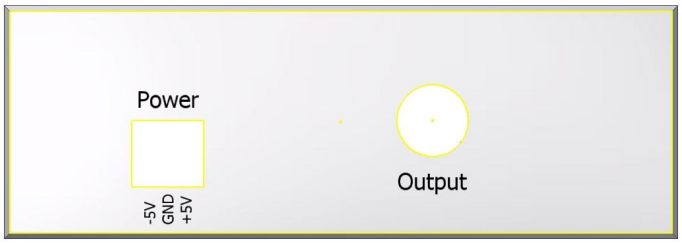

Figure 13c. Rear Label

7. Parts Lists

Designator	Comment	Description	Footprint	Quantity
C1, C2, C33, C40	2.2p	Capacitor SM	0805 (2012)	4
C3, C5, C13, C14, C15, C19, C34, C41, C59, C61	2u2	Capacitor	TANT A (3216)	10
C4, C6, C16, C23, C24, C25, C30, C31, C32, C35, C36, C38, C42, C43, C45, C46, C47, C51, C53, C54, C55, C56, C58, C60, C63, C65, C67, C69, C70, C72, C73, C74, C75	100n	Capacitor SM	0805 (2012)	33
C7, C8, C10, C11, C17, C18	1nF	Capacitor SM	0805 (2012)	6
C9, C26, C29	1u	Capacitor SM	0805 (2012)	3
C12, C68, C71	22p	Capacitor SM	0805 (2012)	3
C20, C21, C22, C57	2p2	Capacitor SM	0805 (2012)	4
C27, C28	100p	Capacitor SM	0805 (2012)	2
C37, C39	10n	Capacitor SM	0805 (2012)	2
C44	33p	Capacitor SM	0805 (2012)	1
C48, C49, C50, C52	10p	Capacitor SM	0805 (2012)	4
C62, C64, C66	10uF	Capacitor	TANT B (3528)	3
D1, D2	BAT54	Schottky Diode	SOD3717 (SOD123)	2
LK1, LK2, LK3, LK4, LK5, LK6, LK7, LK8, LK9, LK10, LK11, LK12, LK13, LK14, LK15, LK16	LINK	2 jumperable pin	HDR1X2	16
P1, P6	MC1,5/3-G-3,5	MINI-COMBICON Right Angle Header, 3Way, 3.5mm Pitch	MC1,5/3-G-3,5	2
P2, P3, P4, P5	Header 2	Header 2.54mm Pitch, 2-Pin	HDR1X2	4
R1, R3, R9, R11, R20, R23	4M7	Resistor SM	0805 (2012)	6
R2, R6, R17, R19, R30, R34, R36, R62	25k	Potentiometer	R_TRIMMER_3214W	8
R4, R7, R21, R38, R45	1k	Potentiometer	R_TRIMMER_3214W	5
R5, R8, R18, R22, R39, R46, R60	1M	Resistor SM	0805 (2012)	7
R10, R13, R15, R24, R53, R54, R55, R56, R72	1k	Resistor SM	0805 (2012)	9
R12, R16, R50	100R	Resistor SM	0805 (2012)	3
R14, R25	970R	Resistor SM	0805 (2012)	2
R26, R35	100k	Resistor SM	0805 (2012)	2
R27, R28, R29, R31, R32, R40, R42, R47, R51, R58, R78, R80	10k	Resistor SM	0805 (2012)	12
R33, R43, R52, R82	5k	Resistor SM	0805 (2012)	4
R37, R41, R44, R49	470k	Resistor SM	0805 (2012)	4
R48	500R	Potentiometer	R_TRIMMER_3214W	1
R57	6k8	Resistor SM	0805 (2012)	1
R59, R63, R69	15k	Resistor SM	0805 (2012)	3
R61, R66, R67, R71, R74, R75, R77	10k	Potentiometer	R_TRIMMER_3214W	7
R64, R73	33k	Resistor SM	0805 (2012)	2
R65	75k	Resistor SM	0805 (2012)	1
R68, R70	56k	Resistor SM	0805 (2012)	2
R76, R81	1k2	Resistor SM	0805 (2012)	2
R79	30k	Potentiometer	R_TRIMMER_3214W	1
TP1, TP3, TP4, TP5, TP6, TP7	TESTPOINT	TESTPOINT	TP50	6

U1, U2, U3, U4, U5, U6, U8, U9, U10, U11, U12, U14, U15, U16	AD8055AN	Low Cost, 300MHz Voltage Feedback Amplifier	DIP-8, N-8_A	14
U7	AD835	250MHz Voltage Output 4-Quadrant Multiplier	DIP-8	1
U13	TL084	Low Noise JFET-Input Operational Amplifiers	DIP-14	1
X1, X2, X3	BNC	BNC Connector	BNC PCB HORZ MOUNT	3

8. PCB Assembly Details

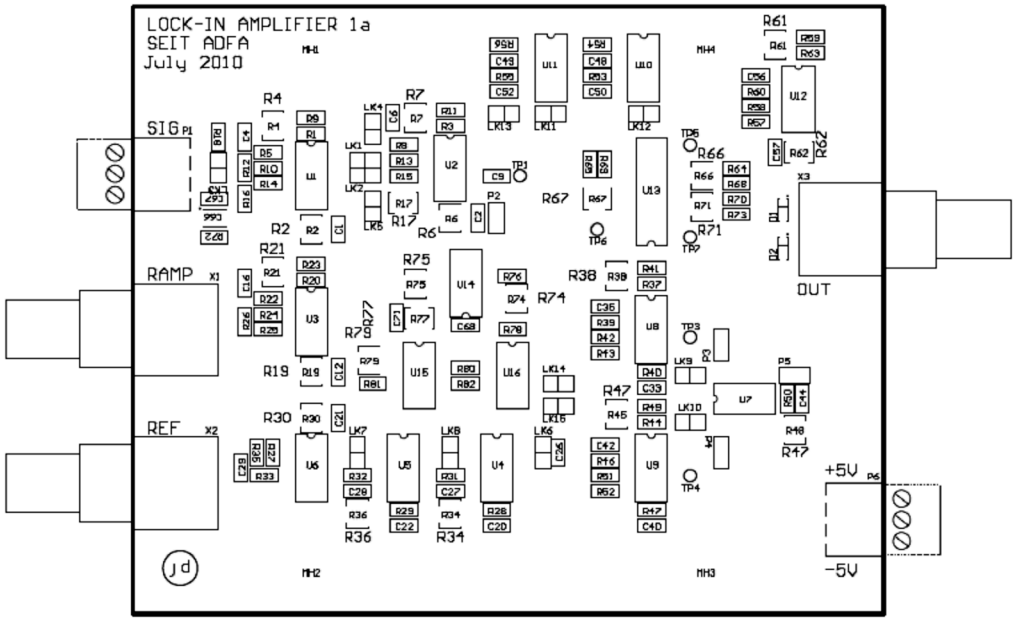

Figure 15. PCB Top Overlay

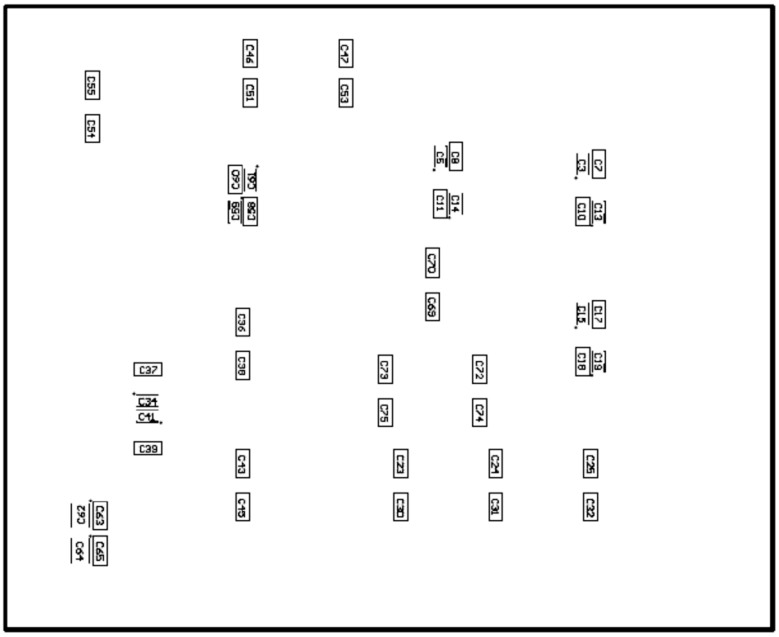

Figure 16. PCB Bottom Overlay